Frictional properties and microstructural evolution of dry and wet calcite-dolomite gouges

Matteo Demurtas[1], Steven A.F. Smith[2], Elena Spagnuolo[3], Giulio Di Toro[3,4]

[1] Physics of Geological Processes, The Njord Centre, Department of Geosciences, University of Oslo, Oslo, Norway
[2] Department of Geology, University of Otago, Dunedin 9054, New Zealand
[3] Istituto Nazionale di Geofisica e Vulcanologia (INGV), Rome 00143, Italy
[4] Dipartimento di Geoscienze, Università degli Studi di Padova, 35131 Padova, Italy

* Corresponding author: Matteo Demurtas (matteodemu@gmail.com)

Key Points

- Presence of water during deformation has a significant effect on the frictional and microstructural evolution of calcite-dolomite gouges
- Gouge fluidization is observed at slip rates of 30 μms^{-1} – 0.1 ms^{-1} under water-dampened conditions
- Development of gouge foliation is observed only at coseismic slip rates and room-humidity conditions

Keywords
Carbonates, earthquake, rock deformation, gouge, calcite, dolomite, friction, microstructure

Abstract

Calcite and dolomite are the two most common minerals in carbonate-bearing faults and shear zones. Motivated by observations of exhumed seismogenic faults in the Italian Central Apennines, we used a rotary-shear apparatus to investigate the frictional and microstructural evolution of c. 3 mm-thick gouge layers consisting of 50 wt.% calcite and 50 wt.% dolomite. The gouges were sheared at a range of slip rates (30 μms^{-1} – 1 ms^{-1}), displacements (0.05–0.4 m), and normal load of 17.5 under both room-humidity and water-dampened conditions. The frictional behaviour and microstructural evolution of the gouges were strongly influenced by the presence of water. At room humidity, slip strengthening was observed up to slip rates of 0.01 ms^{-1}, which was associated with gouge dilation and the development of a 500-900 μm wide slip zone cut by Y-, R-, and R_1-shear bands. Above a slip

Deleted:
Deleted: field examples from
Deleted: investigated
Deleted: mixtures
Deleted: using a rotary-shear apparatus
Deleted: loads (
Deleted: –26 MPa),
Deleted:
Deleted: behaviour

rate of 0.1 ms^{-1}, dynamic weakening accompanied the development of a localised <100 μm thick principal slip zone preserving microstructural evidence for calcite recrystallization and dolomite decarbonation, while the bulk gouges developed a well-defined foliation consisting of organized domains of heavily fractured calcite and dolomite. In water-dampened conditions, evidence of gouge fluidization within a fine-grained principal slip zone was observed at a range of slip rates from 30 μms^{-1} to 0.1 ms^{-1}, suggesting that caution is needed when relating fluidization textures to seismic slip in natural fault zones. Dynamic weakening in water-dampened conditions was observed at 1 ms^{-1}, where the principal slip zone was characterised by patches of recrystallized calcite. However, local fragmentation and reworking of recrystallized calcite suggests a cyclic process involving formation and destruction of a heterogeneous slip zone. Our microstructural data show that development of well-defined gouge foliation under the tested experimental conditions is limited to high-velocity (>0.1 ms^{-1}) and room humidity, supporting the notion that some foliated gouges and cataclasites may form during seismic slip in natural carbonate-bearing faults.

1. Introduction

Calcite and dolomite are the most common minerals in carbonate-bearing faults and shear zones (e.g., Busch and Van Der Pluijm, 1995; Snoke et al., 1998; Bestmann et al., 2000; De Paola et al., 2006; Molli et al., 2010; Tesei et al., 2014; Fondriest et al., 2015, 2020; Delle Piane et al., 2017). In some cases, the distribution and timing of dolomitization plays an important role in controlling strain localization. For example, ductile deformation along the Naukluft Nappe Complex in central Namibia was distributed within a sequence of calcite mylonites, but the main Naukluft Fault localized within dolomitized layers (Viola et al., 2006; Miller et al., 2008).

Although similar in composition, the rheology, deformation mechanisms, and frictional behaviour of calcite and dolomite show important differences. Deformation of calcite has been widely investigated using microstructural analysis (Kennedy and Logan, 1997; Kennedy and White, 2001; Liu et al., 2002; Bestmann et al., 2006; Molli et al., 2011) and laboratory experiments over a wide range of conditions, which includes experiments performed at relatively low strain rates (<10^{-2} s^{-1}), high temperatures (>500 °C), and high pressures (>100 MPa) (e.g., Rutter, 1972; Schmid et al., 1980, 1987; de Bresser et al., 1990; Rutter, 1995; Paterson and Olgaard, 2000), as well as experiments performed at relatively high shear rates (>1 μms^{-1}), low temperatures (<150 °C), and low pressures (<50 MPa) (Smith et al., 2013; Verberne et al., 2014; De Paola et al., 2015; Smith et al., 2015; Rempe et al., 2017; Tesei et al., 2017). Comparatively, the rheology and frictional behaviour of dolomite is relatively poorly

Deleted: wide-
Deleted: -
Deleted: a
Deleted: at these
Deleted: .
Deleted: many
Deleted: where
Deleted: occurs
Deleted: formed
Deleted: heavily
Deleted: Calcite
Deleted: deformation
Deleted: ,
Deleted: ,
Deleted: .
Deleted: and
Deleted: strain
Deleted: ,
Deleted: ,
Deleted: are

understood (e.g., Barber et al., 1981; Weeks and Tullis, 1985). Recently, the importance of dolomite as a fault and shear zone material in sedimentary and metamorphic settings has been emphasized in a number of experimental studies (Austin and Kennedy, 2005; Delle Piane et al., 2007, 2008; Davis et al., 2008; De Paola et al., 2011a, 2011b; Boneh et al., 2013; Fondriest et al., 2013; Holyoke et al., 2014; Green et al., 2015). At low strain rates, dolomite is brittle up to c. 700°C (Kushnir et al., 2015), while calcite can undergo recrystallization at temperatures as low as 150–200°C (Kennedy and White, 2001). This pronounced difference in deformation style under similar ambient conditions may significantly influence the rheology of faults and shear zones in which the two phases co-exist (Oesterling et al., 2007; Kushnir et al., 2015).

Only a few experimental studies have investigated the mechanical behaviour and microstructural evolution of calcite-dolomite mixtures. Experiments have been performed to study the rheological behaviour of mixtures at relatively high pressures and temperatures (e.g., torsion experiments of Delle Piane et al., 2009; Kushnir et al., 2015), as well as the frictional behaviour of mixtures at room temperature over a wide range of strain rates (e.g., room temperature rotary-shear experiments: Mitchell et al., 2015; Smith et al., 2017; Demurtas et al., 2019a,b). In torsion experiments (confining pressures up to 300 MPa, temperatures of 700–800 °C, shear strain rate $\dot{\gamma}$ = 1-3 × 10^{-4} s^{-1}, and finite shear strain $\gamma < 11$), minor quantities of dolomite (e.g., 25 wt.%) in a sintered calcite-rich sample significantly increased the yield strength with respect to pure calcite samples (Kushnir et al., 2015). Under such experimental conditions, two main deformation mechanisms were observed: brittle fracturing in the dolomite grains and ductile flow in calcite, possibly as a result of grain boundary sliding assisted by diffusion creep and dislocation glide (Kushnir et al., 2015). Strain hardening observed in these experiments was interpreted to be due to dolomite grains interrupting more continuous calcite-rich layers and acting as stress concentrators. Brittle failure of dolomite grains eventually allowed the calcite-rich layers to become continuous and to continue deforming by superplastic flow (Kushnir et al., 2015). Although these torsion experiments were performed under significantly elevated temperatures and pressures compared to the experiments in this paper, the results suggest that the occurrence of dolomite in calcite aggregates can influence the mechanical behaviour during deformation.

Mitchell et al. (2015) and Smith et al. (2017) studied the frictional behaviour and microstructural evolution of gouge mixtures (50 wt.% dolomite and 50 wt.% calcite) deformed at low normal stresses ($\sigma_n \leq 17.5$ MPa), high slip rates (V ≥ 0.01 ms^{-1}), and large displacements (d = 0.03-3 m), with the aim of reproducing conditions encountered at the base of fast-moving landslides and during the seismic cycle in shallow-crustal faults. At a slip velocity of 1 ms^{-1}, dynamic weakening was associated with grain size reduction and decarbonation of dolomite

Deleted: .

Deleted: deform plastically

Deleted: . For example, the occurrence of patches or dispersed grains of dolomite within calcite-mylonites can result in more efficient strain localization

Deleted: .

Deleted: .

Deleted: .

within the experimental principal slip zone and in the nearby bulk gouge. During the early stages of these high-velocity experiments, and prior to the onset of dynamic weakening, a well-defined foliation developed within the bulk gouge mixtures due to brittle fracturing of calcite and dolomite accompanied by shearing of the fractured grains in to compositional bands (Mitchell et al., 2015; Smith et al., 2017). These observations indicate that some natural examples of foliated gouges and cataclasites could form during coseismic shearing (Smith et al., 2017), challenging the common interpretation that fault rock foliations result from slow aseismic creep (e.g., Rutter et al., 1986; Chester and Chester, 1998; Lin, 2001; Jefferies et al., 2006). Additionally, Demurtas et al. (2019a) documented the presence of a well-defined crystallographic preferred orientation (CPO) in calcite-dolomite gouges, and interpreted the CPO to result from "brittle" processes involving grain rotation and preferential fracturing along calcite cleavage planes during granular flow at room temperature. Instead, in regions of the mixed gouge layers that experienced substantial frictional heating during high-velocity slip (i.e., within the principal slip zone), Transmission Kikuchi Diffraction analysis suggested that nanogranular aggregates deformed by a combination of grain size sensitive (grains <800 nm) and grain size insensitive (grains >800 nm) plastic creep.

The experimental work summarized above indicates that a diverse range of microstructures can form in calcite-dolomite gouges as a result of both brittle and plastic processes, and that the prevailing microstructures depend on ambient conditions, strain history, and proximity to zones of shear localization and heating. Potentially, this range of microstructures could be recognized in natural gouges and cataclasites, which would provide important insights in to the evolution of slip conditions during the seismic cycle in carbonate-bearing faults. However, to successfully apply the experimental findings to natural fault zones, a more complete picture of microstructural diversity and its dependence on deformation conditions is required. In this context, the aim of this paper is to provide (i) a more comprehensive description of the frictional and microstructural evolution of mixed calcite-dolomite gouges deformed at sub-seismic to seismic slip rates, and (ii) an updated framework for the interpretation of microstructures found in natural calcite- and dolomite-bearing faults.

2. Methods

2.1. Starting materials

Synthetic gouges were prepared by mixing 50 wt.% calcite and 50 wt.% dolomite as previously described in Demurtas et al. (2019a). The calcite-dolomite ratio in the experimental mixtures is similar to that found in natural fault gouges and cataclasites from the Vado di Corno Fault Zone (VCFZ, Italian Central Apennines; Demurtas et al., 2016), and used in previous experimental studies (Smith et al., 2017). The calcite gouge was derived by crushing Carrara marble with a modal composition of 98.8 wt.% calcite and <1 wt.% dolomite and muscovite (see Supplementary Material). The dolomite gouge was derived by crushing dolomitized portions of the Calcare Massiccio Formation from the VCFZ (Demurtas et al., 2016). The crushed gouges were passed through a 250 μm sieve and then mixed together by slow tumbling for c. 30 minutes. Two batches of gouge were prepared (CDM1, calcite = 47.2 wt.% and dolomite = 52.8 wt.%; CDM2, calcite = 42.9 wt.% and dolomite = 57.1 wt.%).

2.2. Experimental setup and deformation conditions

Nineteen experiments were performed at slip rates from 30 μms^{-1} to 1 ms^{-1} with SHIVA (Slow- to HIgh-Velocity rotary-shear friction Apparatus) at the Istituto Nazionale di Geofisica e Vulcanologia in Rome (Di Toro et al., 2010; Niemeijer et al., 2011) (Table 1). The gouges were deformed inside a metal holder specifically designed for incohesive materials (Fig. 1; Smith et al., 2013, 2015). The thickness of the gouge layers at the start of the experiments was c. 3 mm. Horizontal displacements of the axial column were sampled at 2.5 Hz–25 kHz, and measured using a direct current differential transformer (DCDT, 50 mm range and c. 50 µm resolution) and a linear variable differential transformer (LVDT, 3 mm range and c. 0.03 µm resolution). Further details of the data acquisition system, and location and calibration of the load cells, detectors, and devices, are found in Niemeijer et al. (2011) and Smith et al. (2013).

Measurements of room humidity and room temperature were collected at a distance of <1 cm from the gouge holder before and during the experiments (Fig. 1a). Temperature variations during deformation were measured at an acquisition rate of 2.5 Hz using four K-type thermocouples (Nickel-Alumel) installed on the stationary side of the gouge holder (Fig. 1a-b; Demurtas et al., 2019a). One thermocouple was positioned at c. 200 μm from the gouge layer (Fig. 1b). The other three thermocouples were located in the sample holder and stationary column to detect temperature variations due to heat conduction through the gouge holder and apparatus (Fig. 1a). CO_2 emissions were monitored using an OmniStar™ GSD 301 O mass spectrometer designed for gas analysis at atmospheric pressure.

Experiments were performed under both room-humidity and water-dampened conditions at a constant normal stress of 17.5 ± 0.1 MPa (Table 1), the same normal stress used in some previous SHIVA experiments conducted on calcite, dolomite, and calcite-dolomite gouges (Fondriest et al., 2013; Smith et al., 2015, 2017). Room humidity varied between 41% and 62%, and room temperature between 19 °C and 22 °C. In water-dampened conditions, c. 2 ml of deionized water was added to the top of the gouge layer using a pipette before the gouge holder was positioned in the apparatus. Experiment *s1327* was performed

Deleted: at
Deleted:
Deleted: with
Deleted: held constant at
Deleted: , with
Deleted: exception of experiment *s1324* performed at 26 MPa
Deleted: (Table 1).
Deleted: the

using a specially designed water bath that ensured saturation within the gouge layer during this long-duration experiment (Supplementary Material). The gouge holder used in the experiments did not allow us to measure pore-fluid pressure during water-dampened experiments. Experiments were performed at target slip rates ranging from 30 μms^{-1} to 1 ms^{-1}, with acceleration and deceleration of 6 ms^{-2}. Total displacements ranged from 0.05 m to 0.4 m. Two compaction experiments were performed by applying a normal stress of 17.5 MPa for 300 s (i.e., static load experiments in Table 1) and used as references for the microstructure of the starting materials.

2.3 Analytical techniques

After each experiment, the entire gouge layer was recovered and impregnated in low-viscosity epoxy (Araldite 2020) for microstructural analysis. Polished thin sections were cut perpendicular to the gouge layer and subparallel (i.e., tangential cut) to the slip direction (Fig. 1d). Microstructural analysis was performed with a Zeiss Sigma VP Field-Emission Scanning Electron Microscope (SEM) at the Otago Micro and Nanoscale Imaging facility (OMNI; University of Otago. Acquisition conditions for backscattered electron images: accelerating voltage 15 kV, working distance 6-7 mm). Energy-dispersive X-ray spectroscopy (EDS) in the SEM was used to produce element maps showing the distribution of calcium and magnesium, which highlights the distribution of calcite and dolomite. Crystallographic orientation data from calcite were acquired by electron backscatter diffraction (EBSD) on SYTON-polished thin sections. Data were collected with a NordlysF EBSD camera from Oxford Instruments and processed using AZtec software (Oxford Instruments). Mineralogical changes that occurred during the experiments were determined by semi-quantitative X-ray powder diffraction (XRPD) conducted in the Department of Geoscience, University of Padova. The XRPD analyses were performed on both the bulk gouges and on small intact chips of the localized slip surfaces that formed in the experiments.

3. Results

3.1. Friction evolution with slip and slip rate

The evolution of the effective friction coefficient (μ) with slip and slip rate was influenced by the availability of water during deformation (Figs. 2, 3). In room-humidity conditions and slip rates of $\leq$0.01 ms^{-1}, the calcite-dolomite mixtures showed a progressive increase of μ (slip strengthening behaviour) up to 0.75-0.80 (measured between 0.15 m and 0.35 m of slip) following an initial peak fiction (μ_{peak}) of 0.64-0.71 (Figs. 2, 3). At a slip rate of 0.1 ms^{-1}, a substantial decrease of μ was observed (slip weakening behaviour to steady state μ_{ss} of

0.55±0.01) following a prolonged initial strengthening phase (c. 0.062 m) that reached μ_{peak} of 0.68 (Fig. 2b). Significant dynamic weakening was observed at a slip rate of 1 ms^{-1}, following a short initial strengthening phase (lasting c. 0.005 m) that was followed by steady state μ_{ss} of 0.28 (Figs. 2a, 3b). A re-strengthening phase (final μ up to c. 0.56) was observed during deceleration of the rotary column.

Deleted: at 17.5 MPa and 26 MPa normal stress (experiments *s1221* and *s1324*, respectively),
Deleted: -0.008
Deleted: a
Deleted: of
Deleted: 25-0.
Deleted: In these two experiments, a
Deleted: -0.59

In water-dampened conditions, the gouge mixtures showed a similar evolution of friction at slip rates ≤ 0.1 ms^{-1}, characterized by slight slip strengthening to slip neutral behaviour (Fig. 2c). Notably, μ_{peak} and μ_{ss} were lower than in room-humidity experiments, with μ_{peak} = 0.61-0.64 and μ_{ss} = 0.62-0.70 (Fig. 3). At a slip rate of 1 ms^{-1}, the initial strengthening phase was much shorter than in room-humidity conditions (c. 0.003 m), and dynamic weakening resulted in μ_{ss} of 0.31±0.02. Re-strengthening was also observed during deceleration, with an increase in μ up to 0.57.

Deleted:
Deleted: resultsed

3.2. Gouge thickness evolution with slip rate

No significant gouge loss was observed during the experiments, with the exception of those performed at V = 0.1 ms^{-1} discussed below. Therefore, the evolution of axial displacement is interpreted to result from changes in gouge layer thickness due to dilation and compaction. In room-humidity conditions, the evolution of gouge layer thickness depends on slip rate (Fig. 4a). At V ≤ 0.001 ms^{-1}, the gouge layers show a three-stage evolution: (i) initial compaction of c. 90-120 μm at the onset of sliding, (ii) dilation of c. 50-70 μm during the slip strengthening phase, and (iii) approximately constant thickness once the steady state friction coefficient is reached. Overall compaction of c. 30-60 μm is recorded. At V = 0.01 ms^{-1}, after a short lived dilatancy phase (inset in Fig. 4a), compaction of 100 μm is followed by approximately constant thickness (Fig. 4a). At higher slip rates (V ≥ 0.1 ms^{-1}), continuous compaction was observed throughout the experiments (up to c. 300 μm of axial shortening at V = 1 ms^{-1}), and compaction rate increased with slip rate (Fig. 4a).

Deleted:
Deleted: initial

Under water-dampened conditions, the gouge mixtures exhibit a similar evolution of thickness irrespective of slip rate (Fig. 4b). Compaction was initially rapid in the first few cm of sliding, and then reached an approximately constant compaction rate that was similar in all experiments. Total compaction of c. 200-250 μm was recorded (Fig. 4b).

3.3. Temperature evolution and CO_2 emissions

Figure 5a shows maximum temperatures measured by the thermocouple located closest to the gouge layers (Fig. 1b; Demurtas et al., 2019a described temperature evolution with slip). The maximum temperature (621 °C) was achieved in experiment *s1221* performed under room-humidity conditions at V = 1 ms^{-1} (Fig. 5a). For the same slip rate and normal stress, but in water-dampened conditions, the maximum temperature was 210 °C (Fig. 5a). Temperature increases were detected in all experiments at slip rates ≥ 0.01 ms^{-1}, and the maximum temperature increased with increasing slip rate (Fig. 5a).

Because the OmniStar mass spectrometer acquisition system used to detect CO_2 emissions is independent from the control system on SHIVA, CO_2 emissions are plotted simply against the time (in seconds) at which the mass spectrometer was started, which is variable for each experiment (Fig. 5b). CO_2 emissions above ambient levels were only detected in experiments at slip rates ≥ 0.1 ms^{-1} (Fig. 5b). Because the mass spectrometer was not calibrated and the sample holder was open to the laboratory, the data can only be used in a qualitative way. In room-humidity conditions, the intensity of the CO_2 peak was significantly higher at 1 ms^{-1} than at 0.1 ms^{-1}. In water-dampened conditions, the CO_2 peaks were substantially smaller than at equivalent room-humidity conditions.

3.4. Mineralogy of deformed gouges

Compared to the starting materials, no mineralogical changes were detected in any of the deformed bulk gouges (see Supplementary Material). In room-humidity experiment *s1210* (30 μms^{-1}), a slight broadening of the main peak for calcite was observed (Fig. 6a), and to a lesser degree also for dolomite. XRPD analysis of cohesive chips recovered from the slip surface of water-dampened experiment *s1214* (V = 30 μms^{-1}) indicates the presence of aragonite (Fig. 6b). At V = 1 ms^{-1} and room-humidity conditions (experiment *s1221*), the recovered slip surface was composed of dolomite, Mg-calcite, and periclase (MgO) (Fig. 6c). Mg-calcite and periclase are two of the main products of dolomite decarbonation that starts at c. 550 °C ($MgCa(CO_3)_2 \Rightarrow MgO + (Ca,Mg)CO_3 + CO_2$, Samtani et al., 2002; De Paola et al., 2011a,b).

3.5. Microstructures of deformed gouge layers

3.5.1. Microstructures of room-humidity experiments

At slip rates ≤ 0.01 ms^{-1}, gouges were characterized by the development of a 500-900 μm thick slip zone (Figs. 7a and 8), consisting of a fine-grained matrix (grain size c. 1 μm) containing subrounded grains of dolomite c. 5-10 μm in size (Fig. 7b). The slip zone contains sub-parallel, 10-30 μm thick Y, R, and R_1 type shear bands (using the terminology of Logan et al., 1979; Fig. 7a,c). Each individual shear band is associated with a very fine-grained matrix (grain size <1 μm) composed of calcite and dolomite. The presence of multiple interlinked shear bands contributes to a weak foliation within the slip zone that lies sub-parallel to gouge

Deleted:

Deleted:

Deleted:

Deleted:

Deleted:

Deleted: ,

Deleted: Figure 7 summarizes the range of microstructures that developed in room humidity and water-saturated conditions at different slip rates. As noted in previous experiments (e.g. Kitajima et al., 2010; Smith et al., 2017), several distinct microstructures and microstructural domains were recognized, defined by variations in grain size, fabric, and the presence of localized slip surfaces. In the present set of experiments, the microstructural domains and the principal slip zone varied in thickness at different slip rates (Fig. 7). In Figure 8, the thickness of the principal slip zone has been tracked at different deformation conditions (i.e. slip rate and presence of water).¶
¶

Formatted: Font: Bold

Deleted:

Formatted: Font: Bold

Deleted: Fig. 9a

Deleted: 9b

Deleted: 9a

layer boundaries (Fig. 7a). Y-, R-, and most notably R_1-shears, gradually decrease in abundance with increasing slip rate. The transition from fine-grained slip zone to highly fractured bulk gouge is typically well-defined (see upper part in Fig. 7d). The bulk gouge shows widespread cataclasis and intragranular fracturing, which is focussed preferentially into calcite grains (Smith et al., 2017; Demurtas et al., 2019a). Fractures that cut relatively large grains of calcite in the bulk gouge often exploit cleavage planes (e.g., Fig. 7d; Smith et al., 2017; Demurtas et al., 2019a).

At a slip rate of 0.1 ms^{-1}, the bulk gouge develops a weak foliation defined by compositional banding of heavily fractured calcite- and dolomite-rich domains, which lie adjacent to a localized principal slip zone c. 110 μm thick (Fig. 7e). The foliation is inclined 25-30° to the principal slip surface and appears to form by disaggregation and shearing of originally intact calcite and dolomite grains (Fig. 7e). Locally, the principal slip surface is associated with discontinuous lens-shaped patches (up to 15-20 μm thick) of calcite with irregular boundaries and negligible porosity (Fig. 7f).

In experiments conducted at 1 ms^{-1}, the bulk gouges developed a well-defined foliation across most of the thickness of the layers (Fig. 9; Smith et al. 2017; Demurtas et al. 2019a,b) The foliation is defined by alternating calcite- and dolomite-rich domains inclined at c. 40° to the principal slip surface (Fig. 9a-b), which become progressively rotated as they approach the slip surface (Fig. 9c). Large remnant grains (up to 200 μm) in the bulk gouge are often rimmed by fractured tails of finer-grained aggregates (grain size <10 μm), and resemble mantled porphyroclasts in mylonites (e.g., Snoke et al., 1998; Trouw et al., 2009) (arrow in Fig. 9a). At distances of <400 μm from the principal slip surface, the mean grain size decreases substantially, there are very few large surviving grains (up to c. 100 μm in size), and there is a greater degree of mixing between calcite and dolomite (see more uniform colouring in the upper part of EDS map in Fig. 9b). The principal slip zone consists of a 15-20 μm thick, extremely fine-grained layer (<<1 μm in size) composed of calcite, Mg-calcite, dolomite, and periclase (EDS and XRPD analysis; Figs. 6 and 9c-d). Calcite forms elongate aggregates with negligible porosity that display an aggregate preferred orientation with the long axes sub-parallel to foliation (Fig. 9c-e). Dolomite-rich domains show higher porosity and preserve distinct grain structures (Fig. 9c-d). EBSD analysis of elongate calcite aggregates adjacent to the principal slip zone (Fig. 9e) shows a distinct crystallographic preferred orientation with c-axes inclined sub-perpendicular to gouge layer boundaries (Fig. 9f; see also Demurtas et al., 2019b). Locally, a c. 30-40 μm thick layer adjacent to the principal slip zone includes dolomite grains with diffuse internal cracking, clusters of small holes, and vesicular rims previously

Deleted: 9a
Deleted: 9d
Deleted: .
Deleted: 9d
Deleted: 9e
Deleted: 9e
Deleted: 9f
Deleted: 10a
Deleted: 10c
Deleted: .
Deleted: 10a
Deleted: 10c
Deleted: 10c
Deleted: 10c
Deleted: within
Deleted: 10e
Deleted: 10f
Deleted: Adjacent
Deleted: , a c. 30-40 μm thick layer

interpreted as resulting from degassing during decarbonation of comminuted dolomite grains (Fig. 9c; Mitchell et al., 2015; Demurtas et al., 2019b).

3.5.2. Microstructures of water-dampened experiments

In the bulk gouges, the region furthest from the slip zone is composed of grains that show very limited fracturing and resemble the starting materials (Fig. 10a,d; compare with Fig. 1e). Towards the slip zone, grains are increasingly fractured and become rounder. As in the room-humidity experiments, most of the larger "surviving" grains are composed of dolomite (Fig. 10e), consistent with data showing that calcite undergoes more efficient grain size reduction compared to dolomite (Smith et al. 2017, Demurtas et al., 2019a). Domain boundaries (e.g., between intact bulk gouge and comminuted gouge) are often gradational (Fig. 10d), and the total thickness of the comminuted zone is observed to decrease at higher slip rates (from c. 1500 μm thick at 30 μms^{-1} to c. 150 μm thick at 1 ms^{-1}). The principal slip zone consists of an ultrafine-grained matrix (grain size <1 μm) composed of a mixture of calcite and dolomite, with a few well-rounded surviving dolomite grains up to 20-30 μm in size (Fig. 10b-c). At the lowest slip rate (i.e., 30 μms^{-1}), the principal slip zone has a sharp but wavy boundary (characteristic wavelength of c. 300 μm) with the underlying gouge (Fig. 10d), and contains irregular flame-like structures defined by subtle variations in the content of calcite and dolomite (Fig. 10b). The principal slip zone is cut by discrete slip surfaces oriented subparallel to the boundaries of the gouge (Y-shear, Fig. 10c). Experiments performed at 30 μms^{-1} with increasing displacements (*s1327*, *s1329*, *s1328*, *s1330-s1214* with displacements of 0.05-0.1-0.2-0.4 m, respectively; Table 1) show that the three distinct microstructural domains are already recognizable after <0.05 m of slip (Fig. 10d), and that the final thickness of each microstructural domain is a function of total slip and slip rate. At a slip rate of 0.1 ms^{-1}, the comminuted principal slip zone shows distinct grain size grading, characterized by an abundance of relatively large and angular dolomite particles towards the stationary side of the slip zone, and an absence of such particles towards the rotary side (Fig. 10e). Measurements of the thickness of the principal slip zone at different slip rates (Fig. 8) show a log-linear decrease in thickness from c. 400 μm at 30 μms^{-1} to c. 30 μm at 1 ms^{-1}.

At a slip rate of 1 ms^{-1}, the gouge contains an intensely comminuted c. 300-400 μm thick layer bordering the principal slip zone (Fig. 10f). The transition between the two domains is sharp and characterized in places by the occurrence of discrete Y-shears. The principal slip zone consists of lens-shaped patches of a calcite-rich and fine-grained (grain size <1 μm) layer c. 30 μm thick with negligible porosity, which is embedded in a highly comminuted and fine-grained matrix containing a few larger dolomite grains. The principal slip surface cuts sharply

- **Deleted:** 10c; Mitchell et al., 2015; Demurtas et al., 2019b). At 1 ms^{-1} and 26 MPa, the foliation was found only within 400 μm of the principal slip surface (Supplementary Material). The principal slip zone was composed of a calcite-rich recrystallized layer, with substantially reduced porosity and well-rounded dolomite clasts a few micrometres in size (Supplementary Material
- **Formatted:** Font: Bold
- **Deleted:** 11a
- **Deleted:**
- **Deleted:** 11e
- **Deleted:** .
- **Deleted:** 11d
- **Deleted:** 11b
- **Deleted:** .
- **Deleted:** with a
- **Deleted:** 11d
- **Deleted:** 11c
- **Deleted:** displacement
- **Deleted:** displacement
- **Deleted:** 11d
- **Deleted:** -
- **Deleted:** 11e
- **Deleted:** 11f

through this layer and truncates larger clasts (Fig. 10f-g). Locally, reworked angular fragments of the principal slip zone are found (Fig. 10h).

4. Discussion

4.1. Microstructural evolution and weakening mechanisms in calcite-dolomite mixtures

The mechanical behaviour and microstructural evolution of calcite-dolomite gouges show substantial differences based on the availability of water during deformation (Fig. 11). In room-humidity conditions, slip strengthening at slip rates ≤ 0.01 ms^{-1} is associated with (i) initial compaction followed by dilation (Fig. 4a) and (ii) the development of a >500 μm thick slip zone composed of a fine-grained (c. 1 μm) calcite-dolomite mixture cut by Y-, R-, and R_1-shear bands (Fig. 7). These observations have previously been interpreted to relate to the development and broadening of a distributed zone of deformation during strain hardening (e.g., Marone et al., 1990; Beeler et al., 1996; Rathbun and Marone, 2010). This is also supported by widening of the main peaks for calcite and dolomite in XRPD analysis (Fig. 6a), which is interpreted to result from a decrease in the mean crystallite size or deformation-induced microstrain within the crystallites (e.g., Ungár, 2004). A much shorter initial period of dilatancy is observed in experiments performed at V ≥ 0.1 ms^{-1} (Fig. 4a), and this correlates with (i) a transition from slip hardening to slip weakening (Figs. 2-3) and (ii) the development of a well-defined, localized principal slip zone that accommodates most of the strain after it forms (Figs. 7e-f, 9 and 11) (see also Han et al., 2007a; Fondriest et al., 2013; Smith et al., 2013, 2015; Green et al., 2015; De Paola et al., 2015; Mitchell et al., 2015; Rempe et al., 2017; Pozzi et al., 2019; Demurtas et al., 2019b). The switch to slip weakening and a higher degree of strain localization is also associated with a significant temperature rise generated within the principal slip zone (Fig. 5a), CO_2 emissions (Fig. 5b), and the formation of Mg-calcite and periclase in samples collected from the principal slip zone (Fig. 6c). Collectively, these observations suggest that the temperature rise at relatively high slip velocities triggered dynamic weakening and decarbonation of dolomite (and possibly calcite).

At high slip rates (V ≥ 0.1 ms^{-1}), the onset of dynamic weakening in carbonate gouges deformed at room-humidity has been interpreted as a consequence of local heating along incipient slip surfaces, which eventually coalesce into a localized and through-going shear band (De Paola et al., 2015; Smith et al., 2015; Rempe et al., 2017). Further slip then increases the bulk temperature due to continued frictional heating in the principal slip zone and dissipation of heat in to the bulk gouge, resulting in local gouge recrystallization (Smith et al., 2015). Under these conditions, high strain rates can be accommodated by temperature- and grain size-dependent deformation mechanisms leading to “viscous” flow (Green et al., 2015;

Deleted: 11f
Deleted: 11h
Deleted: .
Deleted:
Deleted: 9
Deleted: .
Deleted: .
Deleted: 9e
Deleted: 10
Deleted: friction
Deleted: accompanied by
Deleted: caused
Deleted:

De Paola et al., 2015; Pozzi et al., 2018, 2019; Demurtas et al., 2019b). Demurtas et al. (2019b) performed Transmission Kikuchi Diffraction (TKD) analysis on electron-transparent samples of the low porosity, fine-grained principal slip zone of experiment *s1221* (V = 1 ms^{-1} under room-humidity conditions; Fig. 9c) to investigate the deformation mechanisms active during coseismic sliding in calcite-dolomite mixtures. Their results show that the principal slip zone is composed of a nanogranular aggregate made of two grain populations: (i) nanograins 100-300 nm in size exhibiting low internal lattice distortion, compatible with deformation by grain size sensitive creep, and (ii) nanograins >800 nm in size showing development of subgrains, suggesting deformation by grain size insensitive creep (Demurtas et al., 2019b). Although the maximum temperature measured during deformation in the present experiments was 621 °C (Fig. 5a), accommodation of the calculated strain rates ($\gamma = 6 \times 10^3$ s^{-1}) could be explained by a significant decrease of the activation energy for creep mechanisms (and also decarbonation reactions) due to the nanogranular nature of the particles (Demurtas et al., 2019b). Similar observations were documented by Pozzi et al. (2019) in experimental nanogranular principal slip zones in pure calcite gouges deformed at coseismic slip rates. Alternatively, the temperatures achieved in the slip zones of high velocity (V = 1 ms^{-1}) but short duration experiments (<0.5 s) could be higher than those measured with thermocouples and estimated using numerical models. The thermocouples used here were located a few mm from the edge of the slipping zone (Fig. 1b). Additionally, they have large thermal inertia and low real acquisition rates because the electric potential developing in response to temperature changes is very slow (0.1-0.5 s) compared to the duration of the experiments (c. 0.5 s) (Sarnes and Schrüfer, 2007). Recent studies in which the temperature during experimental seismic slip was measured with optical fibres located inside the slip zone (in-situ measurements at acquisition rates of 1 kHz) detected temperatures 300-400 °C higher than those measured with thermocouples (Aretusini et al., 2019). Temperatures in the slipping zone substantially higher than 621 °C would render grain size- and temperature-dependent deformation mechanisms more efficient. Instead, in the case of experiment *s1218* performed at V = 0.1 ms^{-1}, the moderate dynamic weakening (μ_{ss} = 0.55) can be related to more limited frictional heating within the principal slip zone both in time (max temperature measured of 190 °C, Fig. 5a) and space (patchy recrystallized areas in Fig. 7e-f). However, at least locally, the temperature increase was sufficiently large to decompose dolomite (i.e., c. 550 °C), as testified by the clear CO_2 peak measured during shearing at this velocity (Fig. 5b).

In water-dampened conditions, the mechanical behaviour of the calcite-dolomite mixtures is similar (slight slip strengthening to slip neutral) at all slip rates up to 0.1 ms^{-1} (Fig. 2c). The thickness of the principal slip zone decreases log-linearly with increasing slip rate,

Deleted:
Deleted: 10c
Deleted: the
Deleted: but
Deleted: have been
Deleted: make
Deleted: 9e
Deleted: ,

indicating a progressively higher degree of localization (Fig. 8 and 11). However, this has no obvious effect on the steady state friction coefficient (Fig. 3b), possibly suggesting that the steady state is controlled by strain and that strain is kept constant by microstructural reorganization distributed within the slip zone. The principal slip zone is composed of a very fine-grained (<<1 μm) matrix of calcite and dolomite that includes a few well-rounded dolomite clasts up to 20-30 μm in size (Fig. 10). The similarity in microstructure at all investigated slip rates suggests that water has a major role in promoting faster grain size reduction at the onset of slip, possibly by decreasing the surface energy and yield stress of calcite and dolomite (Risnes et al., 2005; Røyne et al., 2011). XRPD analysis of the slip surface of experiment *s1214* (30 μms^{-1}) showed the formation of aragonite (Fig. 6b). Given that the starting materials were composed of calcite and dolomite only, the aragonite must have formed during deformation. Li et al. (2014) documented polymorphic transformation of calcite into aragonite due to mechanical grinding in a dry (i.e., room humidity) environment. Our observations therefore suggest that relatively dry patches could develop in the gouge layer during slip (or were present at the onset of slip), or that such transformation is also possible under water-dampened conditions.

In water-dampened experiments at 1 ms^{-1}, abrupt dynamic weakening preceded by a very short-lived strengthening phase has previously been documented in experiments on calcite gouges (Rempe et al., 2017, 2020) and calcite marbles (Violay et a., 2014). In gouges, Rempe et al. (2017, 2020) suggested that the rapid onset of dynamic weakening could be related to faster grain size reduction in the presence of water, leading to an early switch from brittle deformation to grain size sensitive creep in the principal slip zone, analogous to the processes suggested to occur in dry gouges (De Paola et al., 2015; Demurtas et al., 2019b; Pozzi et al., 2019). However, there is an apparent discrepancy between the relatively low maximum temperature measured close to the principal slip zone in water-dampened experiments (200 °C at V = 1 ms^{-1}; Fig. 5a), and the observed CO_2 production (Fig. 5b) combined with microstructural evidence for recrystallization during deformation (Fig. 10f-g). As previously discussed, this could be due to an underestimate of the peak temperature (Aretusini et al., 2019). Alternatively, vaporization of water during coseismic sliding could buffer the temperature due to the endothermic nature of the phase transition (Chen et al., 2017a, b). If the pore pressure increase is sufficiently large, then fluids (and vapour) could pressurize the gouge layers and play an important role during dynamic weakening. Finally, Ohl et al. (2020) proposed that mechanical liming (see Martinelli and Plescia, 2004) along natural faults could be a possible slip weakening mechanism that does not necessarily involve a macroscopic temperature increase of >500-600 °C.

Deleted: 11

Deleted:),

Deleted: .

Deleted: saturated

Moved (insertion) [1]

Moved (insertion) [2]

Moved (insertion) [3]

Moved (insertion) [4]

Moved (insertion) [5]

Moved (insertion) [6]

Moved (insertion) [7]

4.2. Implications for natural fault zones

4.2.1 Gouge fluidization at slip rates between 30 μms^{-1} and 0.1 ms^{-1}

The slip zone of the water-dampened experiment performed at 30 μms^{-1} is characterized by flame-like structures, and domain boundaries that display a characteristic wavelength (Figs. 10b,d, 11). Similar structures are typical of soft sediment deformation (Allen, 1985) and have also been described within fault cores (Brodsky et al., 2009), where they are interpreted to result from grain mobilization promoted by fluid overpressure and a difference in viscosity between two adjacent layers during deformation. Additionally, the occurrence of grain size grading within the water-dampened principal slip zone formed at 0.1 ms^{-1} is indicative of grain rearrangement due to frictional sliding (see Masoch et al., 2019 and reference therein), referred to as the "Brazil nut" effect, a phenomenon observed when large grains move to the top of a fluidized layer due to differences in dispersal pressure between large and small particles (Williams, 1976). Grain size grading was reported by Boullier et al. (2009) from the principal slip zone of the 1999 M_w 7.6 Chi-Chi earthquake in Taiwan, and from exhumed normal faults in Alpine Corsica (Masoch et al., 2019). Additionally, similar microstructures were produced by Boulton et al. (2017) in high velocity rotary-shear experiments (V = 1 ms^{-1}) performed on clay-rich drill chips retrieved from the Alpine Fault (New Zealand). As in the experiments by Boulton et al. (2017), grain size grading in our experiments was observed only in water-dampened conditions. Collectively, the presence of flame-like structures, undulating domain boundaries with a characteristic wavelength, and grain size grading, suggests that water-dampened gouges experienced fluidization at slip rates between 30 μms^{-1} and 0.1 ms^{-1}. This is significant because textures and microstructures related to fluidization in natural gouges and cataclasites are often interpreted to form during coseismic slip at high velocities (e.g., Monzawa and Otsuki, 2003; Rowe et al., 2005; Boullier et al., 2009; Brodsky et al., 2009; Demurtas et al., 2016; Boulton et al., 2017; Smeraglia et al., 2017). However, our observations suggest that fluidization might occur at lower slip velocities if local fluid pressures can build up in deforming gouge layers, and may not necessarily be an indicator of coseismic slip.

Various mechanisms have been proposed to account for fluidization of granular materials in fault zones, including (i) frictional heating and thermal pressurization (Boullier et al., 2009), (ii) dilation that limits grain-grain contacts (Borradaile, 1981; Monzawa and Otsuki, 2003), and (iii) focussed fluid flow along slip zones during and after coseismic sliding (e.g., fault-valve mechanism of Sibson, 1990). In our experiments, temperature measurements made during slip at 30 μms^{-1} suggest that significant frictional heating is unlikely, and therefore thermal pressurization is an unlikely mechanism within the slip zone. Water-dampened

Formatted: Indent: First line: 1,27 cm
Formatted: Font: Not Italic, English (US)
Deleted: Fig. 11b
Deleted: fluid
Deleted: a slip rate of
Deleted: -
Deleted: .
Deleted: 2017).
Deleted: .

experiments are characterized by continuous compaction, which also excludes the dilation-related hypothesis of Borradaile (1981). The rapid grain size reduction occurring at the onset of slip, in particular for calcite, creates a principal slip zone that could readily accommodate continuous compaction. Within the principal slip zone, local variations in grain size could create transient differences in gouge permeability that may promote pore fluid pressure build up. A sudden release of fluid from pressurized patches could result in gouge mobilization and injection of material into the adjacent regions. Such variations in permeability and pore pressure are likely to occur on a local level that may not be recorded by bulk variations of gouge thickness during deformation.

4.2.2 Foliation development in calcite-dolomite gouges at coseismic slip rates

Foliated gouges and cataclasites are common fault rocks in the brittle upper crust (Snoke et al., 1998). Typically, they are interpreted to form due to a combination of cataclasis and dissolution-precipitation reactions during aseismic fault creep (e.g., Rutter et al., 1986; Chester and Chester, 1998; Lin, 2001; Collettini and Holdsworth, 2004; Jefferies et al., 2006; De Paola et al., 2008; Wallis et al., 2013). Experimental observations support this idea, and show that well-defined foliations can form as a result of dissolution-precipitation reactions accompanied by granular flow and frictional sliding at low slip rates ($V < 1$ μms^{-1}; Bos et al., 2000; Niemeijer and Spiers, 2006).

However, the association of foliated fault rocks with possible microstructural indicators of seismic slip in natural fault rocks (e.g., slip zones containing recrystallized material, see Demurtas et al., 2016) led Smith et al. (2017) to investigate the possibility that some foliated gouges and cataclasites might have a coseismic origin. Rotary-shear experiments performed at a slip rate of 1.13 ms^{-1} on gouges composed of 50 wt.% calcite and 50 wt.% dolomite showed the development of a foliation defined by an organized banding of heavily fractured calcite and dolomite clasts (Smith et al., 2017). Experiments performed at increasing displacements revealed that the foliations are established during the initial strengthening phase, when distributed strain throughout the bulk gouge causes grain comminution and distributed shearing. Once dynamic weakening occurs, strain progressively localizes into a single continuous principal slip zone, and the foliation in the bulk gouge does not show any further microstructural change. Shear strain analysis of the foliated layers showed that relatively low values of strain ($\gamma < 4$) are needed to develop a foliation. Based on their observations, Smith et al. (2017) suggested that some natural foliated gouges and cataclasites characterized by compositional banding, grain size variations, and preferred particle or fracture alignments, could form by distributed brittle flow as strain localizes during coseismic shearing, especially if

Deleted: We propose that fluidization in

Deleted: might be caused by local fluid pressure increase within water-saturated patches as a result of

Deleted: combined with minimal fluid loss during deformation.

Deleted: water

Deleted: the

Deleted: patch

Deleted: in to

Deleted: slip zone

Moved up [1]: In water-dampened experiments at 1 ms^{-1}, abrupt dynamic weakening preceded by a very short-lived strengthening phase has previously been documented in experiments on calcite gouges (Rempe et al.,

Deleted: 2017

Moved up [2]:) and calcite marbles (Violay et a., 2014). In

Moved up [3]: In gouges, Rempe et al.

Deleted: (2017) suggested that the rapid onset of dynamic weakening could be related to faster grain size reduction in the presence of water, leading to an early switch from brittle deformation to grain size sensitive creep in the principal slip zone, analogous to the process

Moved up [4]: suggested to occur in dry gouges (De Paola et al., 2015; Demurtas et al., 2019b; Pozzi et al., 2019).

Moved up [5]: 2019). However, there is an apparent discrepancy between the relatively low maximum temperature measured close to the principal slip zone in water-dampened experiments (200 °C at V = 1 ms^{-1}; Fig. 5a), and the observed CO_2 production (Fig. 5b) combined with microstructural evidence for recrystallization during deformation (Fig.

Deleted: 11f-g). As previously discussed, this could be due to an underestimate of

Moved up [6]: peak temperature (Aretusini et al., 2019).

Deleted: Alternatively, Ohl et al. (2019

Moved up [7]:) proposed that mechanical liming (see Martinelli and Plescia, 2004) along natural faults could be a possible slip weakening mechanism that does not necessarily involve a macroscopic temperature increase of >500-600 °C.¶
¶
4.2.

Formatted: Font: Not Italic, English (US)

Deleted: .

Deleted: . mirror-like

Deleted: surfaces with truncated clasts such foliations are found in proximity to microstructural indicators of coseismic slip. The experiments presented in this paper allow us to test this hypothesis over a wider range of slip rates (i.e., 30 μms^{-1} – 1 ms^{-1}) and deformation conditions (i.e., room humidity vs. water dampened). In these new experiments, the formation of well-defined foliations throughout the bulk gouge was only observed at high slip rates (V = 1 ms^{-1}) and room-humidity conditions (Figs. 9, 11), corresponding to the conditions presented in Smith et al. (2017). Local foliation development was also observed in lower velocity experiments at room humidity, although this was restricted to regions <400 μm from the principal slip surface (Fig. 7e).

Our new experiments support the hypothesis presented in Smith et al. (2017) that well-defined foliations in calcite-dolomite gouges can form during high velocity sliding in carbonate gouges, and could be used in conjunction with other microstructures (e.g., seismic slip indicators) to better understand localization processes in faults. The lowest slip velocity studied here (i.e., 30 μms^{-1}) is still too high for pressure-solution to be efficient in calcite or dolomite at room temperature. Lower slip rates might promote the activation of pressure-solution, which could result in the formation of a foliation under certain conditions. Grain elongation and foliation development have previously been reported in experiments performed on calcite-dolomite mixtures by Delle Piane et al. (2009) and on calcite by Verberne et al. (2017). However, in the former case, the deformation conditions (i.e., torsion experiments at temperatures of 700-800 °C, confining pressure of 300 MPa, shear strain rate of 3 × 10^{-4}-10^{-5} s^{-1}) were representative of mid- to lower crustal depths, rather than the low-pressure low-temperature ambient conditions explored here. Although the slip rates in Verberne et al. (2017) were closer to the ones explored in this study (i.e., 1 nms^{-1} to 100 μms^{-1}), the temperature (T = 550 °C) and stress conditions (effective normal stress of 50 MPa and pore fluid pressure of 100 MPa) were designed to investigate the ductile-brittle transition at the base of the seismogenic zone rather than shallow faulting.

5. Conclusions

A series of rotary-shear experiments was performed on gouges composed of 50 wt.% calcite and 50 wt.% dolomite to develop an understanding of microstructural evolution at a range of slip rates (30 μms^{-1} – 1 ms^{-1}), fluid conditions (room humidity and water dampened), total displacements (0.05–0.4 m), and normal load of 17.5 MPa.

The evolution of the apparent friction coefficient is strongly influenced by the presence of water. Under room humidity conditions, slip strengthening is observed up to slip rates of 0.01 ms^{-1}, above which dynamic weakening occurs. In water-dampened conditions, slight slip strengthening to slip neutral friction characterises experiments up to slip velocities of 0.1 ms^{-1},

Deleted: .
Deleted: .
Deleted: The
Deleted:
Deleted: Fig. 10
Deleted: 9e
Deleted: .
Deleted: .
Deleted:).
Deleted: this
Deleted: .
Deleted: /-
Formatted: English (US)
Deleted: loads (
Deleted: and 26
Deleted:).
Deleted: : at

above which dynamic weakening occurs abruptly. The mechanical differences observed under room humidity and water-dampened conditions are also reflected in the microstructures of the deformed gouge layers. At room humidity, slip strengthening is associated with diffuse deformation and the development of a relatively thick slip zone cut by Y-, R-, and R_1-shear bands. The onset of dynamic weakening is concomitant with the development of a localised principal slip zone containing evidence of dolomite decarbonation and calcite recrystallization. In the presence of water, evidence of gouge fluidization within a fine-grained principal slip zone is observed at slip rates from 30 μms^{-1} to 0.1 ms^{-1}, suggesting that fluidization may not be restricted to coseismic slip rates. At 1 ms^{-1}, the principal slip zone is characterised by patches of recrystallized calcite that are locally broken and reworked.

The development of a well-defined foliation in the bulk gouge layer only occurs in room humidity experiments at a slip rate of 1 ms^{-1}, consistent with the work of Smith et al. (2017). This observation supports the notion that some foliated gouges and cataclasites may form during coseismic slip in natural carbonate-bearing faults.

Acknowledgements

MD, ES and GDT were supported by the European Research Council Consolidator grant project 614705 NOFEAR. SAFS acknowledges the Marsden Fund Council (projects UOO1417 and UOO1829) administered by the Royal Society of New Zealand. Stefano Aretusini and Michele Fondriest are thanked for fruitful discussions. Marianne Negrini provided assistance with the SEM and EBSD data processing in the Otago Centre for Electron Microscopy, University of Otago. Federico Zorzi is thanked for performing the XRPD analysis and Leonardo Tauro for assistance during thin section preparation. We thank the Editor Florian Fusseis and Bart Verberne and John Bedford for constructive review that improved the final version of the manuscript.

References

Allen, J.R.L., 1985. Principles of Physical Sedimentology. George Allen and Unwin, Boston, 272 pp.

Aretusini S., A. Nuñez Cascajero, E. Spagnuolo, A. Tapetado, C. Vazquez, G. Di Toro, 2019. How hot is a lab-earthquake? American Geophysical Union Fall Meeting Abstract 519812, M23E-0160, San Francisco (USA), December 2019.

Austin, N.J., Kennedy, L.A., 2005. Textural controls on the brittle deformation of dolomite: Variations in peak strength. In: Gapais, D., Brun, J.P., Cobbold, P.R. (Eds.), Deformation Mechanisms, Rheology and Tectonics: From Minerals to the Lithosphere. Geological Society, London, Special Publications, 37–49. https://doi.org/10.1144/GSL.SP.2005.243.01.05

Barber, D. J., Heard, H. C., and Wenk, H. R., 1981. Deformation of dolomite single-crystals from 20-800 degrees-C: Physics and Chemistry of Minerals, v. 7, no. 6, p. 271-286.

Beeler, N.M., Tullis, T.E., Blanpied, M.L., Weeks, J.D., 1996. Frictional behavior of large displacement experimental faults. Journal of Geophysical Research: Solid Earth 101, 8697–8715. https://doi.org/10.1029/96JB00411.

Bestmann, M., Kunze, K., Matthews, A., 2000. Evolution of a calcite marble shear zone complex on Thassos Island, Greece: Microstructural and textural fabrics and their kinematic significance. Journal of Structural Geology 22, 1789–1807. https://doi.org/10.1016/S0191-8141(00)00112-7.

Bestmann, M., Prior, D.J., Grasemann, B., 2006. Characterisation of deformation and flow mechanics around porphyroclasts in a calcite marble ultramylonite by means of EBSD analysis. Tectonophysics 413, 185–200. https://doi.org/10.1016/j.tecto.2005.10.044.

Boneh, Y., Sagy, A., Reches, Z., 2013. Frictional strength and wear-rate of carbonate faults during high-velocity, steady-state sliding. Earth Planet. Sci. Lett., 381, 127–137, doi:10.1016/j.epsl.2013.08.050.

Borradaile, G.J., 1981. Particulate flow of rock and the formation of cleavage. Tectonophysics 72, 305–321.

Bos, B., Peach, C.J., Spiers, C.J., 2000. Frictional-viscous flow of simulated fault gouge caused by the combined effects of phyllosilicates and pressure solution. Tectonophysics 327, 173–194.

Boullier, A.M., Yeh, E.C., Boutareaud, S., Song, S.R., Tsai, C.H., 2009. Microscale anatomy of the 1999 Chi-Chi earthquake fault zone. Geochemistry, Geophysics, Geosystems 10. https://doi.org/10.1029/2008GC002252.

Boulton, C., Yao, L., Faulkner, D.R., Townend, J., Toy, V.G., Sutherland, R., Ma, S., Shimamoto, T., 2017. High-velocity frictional properties of Alpine Fault rocks: Mechanical data, microstructural analysis, and implications for rupture propagation. Journal of Structural Geology 97, 71–92. https://doi.org/10.1016/j.jsg.2017.02.003.

Formatted: Norwegian Bokmål

Moved down [8]: Brodsky, E.E., Rowe, C.D., Meneghini, F., Moore, J.C., 2009. A geological fingerprint of low-viscosity fault fluids mobilized during an earthquake. Journal of Geophysical Research: Solid Earth 114, 1–14. https://doi.org/10.1029/2008JB005633.

Brodsky, E.E., Rowe, C.D., Meneghini, F., Moore, J.C., 2009. A geological fingerprint of low-viscosity fault fluids mobilized during an earthquake. Journal of Geophysical Research: Solid Earth 114, 1–14. https://doi.org/10.1029/2008JB005633.

Busch, J.P., van der Pluijm, B.A., 1995. Calcite textures, microstructures and rheological properties of marble mylonites in the Bancroft shear zone, Ontario, Canada. Journal of Structural Geology 17, 677–688. https://doi.org/10.1016/0191-8141(94)00092-E.

Chen, J., Niemeijer, A.R., Fokker, P.A., 2017. Vaporization of fault water during seismic slip. Journal of Geophysical Research: Solid Earth 122, 4237–4276. https://doi.org/10.1002/2016JB013824.

Chen, J., Niemeijer, A., Yao, L., Ma, S., 2017. Water vaporization promotes coseismic fluid pressurization and buffers temperature rise. Geophysical Research Letters 44. https://doi.org/10.1002/2016GL071932.

Chester, F.M., Chester, J.S., 1998. Ultracataclasite structure and friction processes of the Punchbowl fault, San Andreas system, California. Tectonophysics 295, 199–221. https://doi.org/10.1016/S0040-1951(98)00121-8.

Collettini, C., Holdsworth, R.E., 2004. Fault zone weakening and character of slip along low-angle normal faults: insights from the Zuccale fault, Elba, Italy. Journal of the Geological Society 161, 1039–1051.

Davis, N.E., Kronenberg, A.K., Newman, J., 2008. Plasticity and diffusion creep of dolomite. Tectonophysics 456, 127–146. https://doi.org/10.1016/j.tecto.2008.02.002.

De Bresser, J.H.P., Spiers, C.J., 1990. High-temperature deformation of calcite single crystals by r+ and f+ slip. In: Knipe, R.J., Rutter, E.H. (Eds.), Geological Society Special Publication. Geological Society Special Publication, 285–298. https://doi.org/10.1144/GSL.SP.1990.054.01.25.

De Paola, N., Mirabella, F., Barchi, M.R., Burchielli, F., 2006. Early orogenic normal faults and their reactivation during thrust belt evolution: the Gubbio Fault case study, Umbria-Marche Apennines (Italy). Journal of Structural Geology 28, 1948–1957. https://doi.org/10.1016/j.jsg.2006.06.002.

De Paola, N., Collettini, C., Faulkner, D.R., Trippetta, F., 2008. Fault zone architecture and deformation processes within evaporitic rocks in the upper crust. Tectonics 27, 1–21. https://doi.org/10.1029/2007TC002230.

De Paola, N., Chiodini, G., Hirose, T., Cardellini, C., Caliro, S., Shimamoto, T., 2011a. The geochemical signature caused by earthquake propagation in carbonate-hosted faults. Earth and Planetary Science Letters 310, 225–232. https://doi.org/10.1016/j.epsl.2011.09.001.

De Paola, N., Hirose, T., Mitchell, T., Di Toro, G., Viti, C., Shimamoto, T., 2011b. Fault lubrication and earthquake propagation in thermally unstable rocks. Geology 39, 35–38. https://doi.org/10.1130/G31398.1.

De Paola, N., Holdsworth, R.E., Viti, C., Collettini, C., Bullock, R., 2015. Can grain size sensitive flow lubricate faults during the initial stages of earthquake propagation? Earth and Planetary Science Letters 431, 48–58. https://doi.org/10.1016/j.epsl.2015.09.002.

Moved (insertion) [8]

Formatted: Norwegian Bokmål

Delle Piane, C., Burlini, L., Grobety, B., 2007. Reaction-induced strain localization: Torsion experiments on dolomite. Earth and Planetary Science Letters 256, 36–46. https://doi.org/10.1016/j.epsl.2007.01.012.

Delle Piane, C., Burlini, L., Kunze, K., Brack, P., Burg, J.P., 2008. Rheology of dolomite: Large strain torsion experiments and natural examples. Journal of Structural Geology 30, 767–776. https://doi.org/10.1016/j.jsg.2008.02.018.

Delle Piane, C., Burlini, L., Kunze, K., 2009. The influence of dolomite on the plastic flow of calcite. Rheological, microstructural and chemical evolution during large strain torsion experiments. Tectonophysics 467, 145–166. https://doi.org/10.1016/j.tecto.2008.12.022.

Delle Piane, C., Clennell, M. Ben, Keller, J.V.A., Giwelli, A., Luzin, V., 2017. Carbonate hosted fault rocks: A review of structural and microstructural characteristic with implications for seismicity in the upper crust. Journal of Structural Geology 103, 17–36. https://doi.org/10.1016/j.jsg.2017.09.003.

Demurtas, M., Fondriest, M., Balsamo, F., Clemenzi, L., Storti, F., Bistacchi, A., Di Toro, G., 2016. Structure of a normal seismogenic fault zone in carbonates: The Vado di Corno Fault, Campo Imperatore, Central Apennines (Italy). J. Struct. Geol. 90, 185–206. doi:10.1016/j.jsg.2016.08.004.

Demurtas, M., Smith, S.A.F., Prior, D.J., Spagnuolo, E., Di Toro, G., 2019a. Development of crystallographic preferred orientation during cataclasis in low-temperature carbonate fault gouge. Journal of Structural Geology 126, 37–50. https://doi.org/10.1016/j.jsg.2019.04.015.

Demurtas, M., Smith, S.A.F., Prior, D.J., Brenker, F.E., Di Toro, G., 2019b. Grain size sensitive creep during simulated seismic slip in nanogranular fault gouges: constraints from Transmission Kikuchi Diffraction (TKD). Journal of Geophysical Research: Solid Earth 124. https://doi.org/10.1029/2019jb018071.

Di Toro, G., Niemeijer, A.R., Tripoli, A., Nielsen, S., Di Felice, F., Scarlato, P., Spada, G., Alessandroni, R., Romeo, G., Di Stefano, G., Smith, S., Spagnuolo, E., Mariano, S., 2010. From field geology to earthquake simulation: A new state-of-The-art tool to investigate rock friction during the seismic cycle (SHIVA). Rendiconti Lincei 21, 95–114. https://doi.org/10.1007/s12210-010-0097-x.

Fondriest, M., Smith, S.A.F., Candela, T., Nielsen, S.B., Mair, K., Toro, G. Di, 2013. Mirror-like faults and power dissipation during earthquakes. Geology 41, 1175–1178. https://doi.org/10.1130/G34641.1.

Fondriest, M., Aretusini, S., Di Toro, G., Smith, S.A.F., 2015. Fracturing and rock pulverization along an exhumed seismogenic fault zone in dolostones: The Foiana Fault Zone (Southern Alps, Italy). Tectonophysics 654, 56–74. https://doi.org/10.1016/j.tecto.2015.04.015.

Fondriest, M., Balsamo, F., Bistacchi, A., Clemenzi, L., Demurtas, M., Storti, F., Di Toro, G., 2020. Structural Complexity and Mechanics of a Shallow Crustal Seismogenic Source (Vado di Corno Fault Zone, Italy). Journal of Geophysical Research: Solid Earth 125. https://doi.org/10.1029/2019JB018926.

Green II, H.W., Shi, F., Bozhilov, K., Xia, G., Reches, Z., 2015. Phase transformation and nanometric flow cause extreme weakening during fault slip. Nature Geoscience 8, 484–489. https://doi.org/10.1038/ngeo2436.

Han, R., Shimamoto, T., Ando, J., Ree, J.-H., 2007. Seismic slip record in carbonate-bearing fault zones: An insight from high-velocity friction experiments on siderite gouge. Geology 35, 1131–1134. https://doi.org/10.1130/G24106A.1.

Holyoke, C.W., Kronenberg, A.K., Newman, J., 2014. Microstructural evolution during strain localization in dolomite aggregates. Journal of Structural Geology 69, 449–464. doi:10.1016/j.jsg.2014.04.008.

Jefferies, S.P., Holdsworth, R.E., Shimamoto, T., Takagi, H., Lloyd, G.E., Spiers, C.J., 2006. Origin and mechanical significance of foliated cataclastic rocks in the cores of crustal-scale faults: Examples from the Median Tectonic Line, Japan. Journal of Geophysical Research: Solid Earth 111, 1–17. https://doi.org/10.1029/2005JB004205.

Kennedy, L. a., Logan, J.M., 1997. The role of veining and dissolution in the evolution of fine-grained mylonites: the McConnell thrust, Alberta. Journal of Structural Geology 19, 785–797. https://doi.org/10.1016/S0191-8141(97)00005-9.

Kennedy, L.A., White, J.C., 2001. Low-temperature recrystallization in calcite: Mechanisms and consequences. Geology 29, 1027–1030. https://doi.org/10.1130/0091-7613(2001)029<1027:LTRICM>2.0.CO.

Kitajima, H., Chester, J.S., Chester, F.M., Shimamoto, T., 2010. High-speed friction of disaggregated ultracataclasite in rotary shear: Characterization of frictional heating, mechanical behavior, and microstructure evolution. Journal of Geophysical Research: Solid Earth 115, 1–21. https://doi.org/10.1029/2009JB007038.

Kushnir, A.R.L., Kennedy, L.A., Misra, S., Benson, P., White, J.C., 2015. The mechanical and microstructural behaviour of calcite-dolomite composites: An experimental investigation. Journal of Structural Geology 70, 200–216. https://doi.org/10.1016/j.jsg.2014.12.006.

Li, T., Sui, F., Li, F., Cai, Y., Jin, Z., 2014. Effects of dry grinding on the structure and granularity of calcite and its polymorphic transformation into aragonite. Powder Technology 254, 338–343. https://doi.org/10.1016/j.powtec.2014.01.043.

Lin, A., 2001. S-C fabrics developed in cataclastic rocks from the Nojima fault zone, Japan and their implications for tectonic history. Journal of Structural Geology 23, 1167–1178. https://doi.org/10.1016/S0191-8141(00)00171-1.

Liu, J., Walter, J.M., Weber, K., 2002. Fluid-enhanced low-temperature plasticity of calcite marble: Microstructures and mechanisms. Geology 30, 787–790. https://doi.org/10.1130/0091-7613(2002)030<0787:FELTPO>2.0.CO;2.

Logan, J. M., M. Friedman, N. Higgs, C. Dengo, and T. Shimamoto, 1979. Experimental studies of simulated gouge and their application to studies of natural fault zones. Proceedings of Conference VIII on Analysis of Actual Fault Zones in Bedrock, U.S. Geological Survey Open-File Report 79–1239.

Marone, C., Raleigh, C.B., Scholz, C.H., 1990. Frictional behavior and constitutive modeling of simulated fault gouge. Journal of Geophysical Research 95, 7007–7025.

Martinelli, G., Plescia, P., 2004. Mechanochemical dissociation of calcium carbonate: Laboratory data and relation to natural emissions of CO2. Physics of the Earth and Planetary Interiors 142, 205–214. https://doi.org/10.1016/j.pepi.2003.12.009.

Masoch, S., Fondriest, M., Preto, N., Secco, M., Di Toro, G., 2019. Seismic cycle recorded in cockade-bearing faults (Col de Teghime, Alpine Corsica). Journal of Structural Geology 129, 103889. https://doi.org/10.1016/j.jsg.2019.103889.

Miller, J.A., Viola, G., Mancktelow, N.S., 2008. Oxygen, carbon and strontium isotope constraints on the mechanisms of nappe emplacement and fluid-rock interaction along the subhorizontal Naukluft Thrust, central Namibia. Journal of the Geological Society 165, 739–753. https://doi.org/10.1144/0016-76492007-079.

Mitchell, T.M., Smith, S.A.F., Anders, M.H., Di Toro, G., Nielsen, S., Cavallo, A., Beard, A.D., 2015. Catastrophic emplacement of giant landslides aided by thermal decomposition: Heart Mountain, Wyoming. Earth and Planetary Science Letters 411, 199–207. https://doi.org/10.1016/j.epsl.2014.10.051.

Molli, G., Cortecci, G., Vaselli, L., Ottria, G., Cortopassi, A., Dinelli, E., Mussi, M., Barbieri, M., 2010. Fault zone structure and fluid-rock interaction of a high angle normal fault in Carrara marble (NW Tuscany, Italy). Journal of Structural Geology 32, 1334–1348. https://doi.org/10.1016/j.jsg.2009.04.021.

Molli, G., White, J.C., Kennedy, L., Taini, V., 2011. Low-temperature deformation of limestone, Isola Palmaria, northern Apennine, Italy - The role of primary textures, precursory veins and intracrystalline deformation in localization. Journal of Structural Geology 33, 255–270. https://doi.org/10.1016/j.jsg.2010.11.015.

Monzawa, N., Otsuki, K., 2003. Comminution and fluidization of granular fault materials: Implications for fault slip behavior. Tectonophysics 367, 127–143. https://doi.org/10.1016/S0040-1951(03)00133-1.

Niemeijer, A.R., Spiers, C.J., 2006. Velocity dependence of strength and healing behaviour in simulated phyllosilicate-bearing fault gouge. Tectonophysics 427, 231–253. https://doi.org/10.1016/j.tecto.2006.03.048.

Niemeijer, A.R., Di Toro, G., Nielsen, S.B., Di Felice, F., 2011. Frictional melting of gabbro under extreme experimental conditions of normal stress, acceleration, and sliding velocity. Journal of Geophysical Research 116, 1–18. https://doi.org/10.1029/2010JB008181.

Oesterling, N., Heilbronner, R., Stünitz, H., Barnhoorn, A., Molli, G., 2007. Strain dependent variation of microstructure and texture in naturally deformed Carrara marble. Journal of Structural Geology 29, 681–696. https://doi.org/10.1016/j.jsg.2006.10.007.

Ohl, M., Plümper, O., Chatzaras, V., Wallis, D., Vollmer, C., Drury, M., 2019. Mechanisms of fault mirror formation and fault healing in carbonate rocks. Earth and Planetary Science Letters 530, 115886. https://doi.org/10.1016/j.epsl.2019.115886.

Pozzi, G., De Paola, N., Nielsen, S.B., Holdsworth, R.E., Bowen, L., 2018. A new interpretation for the nature and significance of mirror-like surfaces in experimental carbonate-hosted seismic faults. Geology 46, 583–586. https://doi.org/10.1130/G40197.1.

Pozzi, G., De Paola, N., Holdsworth, R.E., Bowen, L., Nielsen, S.B., Dempsey, E.D., 2019. Coseismic ultramylonites: An investigation of nanoscale viscous flow and fault weakening during seismic slip. Earth and Planetary Science Letters 516, 164–175. https://doi.org/10.1016/j.epsl.2019.03.042.

Rathbun, A.P., Marone, C., 2010. Effect of strain localization on frictional behavior of sheared granular materials. Journal of Geophysical Research 115, 1–16. https://doi.org/10.1029/2009JB006466.

Rempe, M., Smith, S., Mitchell, T., Hirose, T., Di Toro, G., 2017. The effect of water on strain localization in calcite fault gouge sheared at seismic slip rates. Journal of Structural Geology 97, 104–117. https://doi.org/10.1016/j.jsg.2017.02.007.

Rempe, M., Di Toro, G., Mitchell, T.M., Smith, S.A.F., Hirose, T., Renner, J., 2020. Influence of Effective Stress and Pore Fluid Pressure on Fault Strength and Slip Localization in Carbonate Slip Zones. Journal of Geophysical Research: Solid Earth 125. https://doi.org/10.1029/2020JB019805.

Risnes, R., Madland, M. V., Hole, M., Kwabiah, N.K., 2005. Water weakening of chalk - Mechanical effects of water-glycol mixtures. Journal of Petroleum Science and Engineering 48, 21–36. https://doi.org/10.1016/j.petrol.2005.04.004.

Røyne, A., Bisschop, J., Dysthe, D.K., 2011. Experimental investigation of surface energy and subcritical crack growth in calcite. Journal of Geophysical Research 116, 10. https://doi.org/10.1029/2010jb008033.

Rowe, C.D., Moore, J.C., Meneghini, F., McKeirnan, A.W., 2005. Large-scale pseudotachylytes and fluidized cataclasites from an ancient subduction thrust fault. Geology 33, 937–940. https://doi.org/10.1130/G21856.1.

Rutter, E.H., 1972. The effects of strain-rate changes on the strength and ductility of Solenhofen limestone at low temperature and confining pressure. International Journal of Rock Mechanics and Mining Sciences 9, 183–189.

Rutter, E.H., Maddock, R.H., Hall, S.H., White, S.H., 1986. Comparative microstructures of natural and experimentally produced clay-bearing fault gouges. Pure and Applied Geophysics 124, 3–30. https://doi.org/10.1007/BF00875717.

Rutter, E.H., 1995. Experimental study of the influence of stress, temperature, and strain on the dynamic recrystallization of Carrara marble. Journal of Geophysical Research 100, 24651. https://doi.org/10.1029/95jb02500.

Samtani, M., Dollimore, D., Alexander, K.S., 2002. Comparison of dolomite decomposition kinetics with related carbonates and the effect of procedural variables on its kinetic parameters. Thermochimica Acta 393, 135–145.

Sarnes, B., Schrüfer, E., 2007. Determination of the time behaviour of thermocouples for sensor speedup and medium supervision. Proceedings of the Estonian Academy of Sciences: Engineering 13, 295–309.

Schmid, S.M., Paterson, M.S., Boland, J.N., 1980. High temperature flow and dynamic recrystallization in Carrara marble. Tectonophysics 65, 245–280.

Formatted: Norwegian Bokmål

Schmid, S.M., Panozzo, R., Bauer, S., 1987. Simple shear experiments on calcite rocks: rheology and microfabric. Journal of Structural Geology 9, 747–778. https://doi.org/10.1016/0191-8141(87)90157-X.

Sibson, R.H., 1990. Conditions for fault-valve behaviour. In: Knipe, R.J., Rutter, E.H. (Eds.), Deformation Mechanisms, Rheology and Tectonics. Geological Society Special Publication, 15–28. https://doi.org/10.1144/GSL.SP.1990.054.01.02.

Smeraglia, L., Billi, A., Carminati, E., Cavallo, A., Doglioni, C., 2017. Field- to nano-scale evidence for weakening mechanisms along the fault of the 2016 Amatrice and Norcia earthquakes, Italy. Tectonophysics 712–713, 156–169. https://doi.org/10.1016/j.tecto.2017.05.014.

Snoke, A.W., Tullis, J., Todd, V.R., 1998. Fault-Related Rocks: a Photographic Atlas. Princeton Univ. Press, Princeton, N.J.

Smith, S.A.F., Di Toro, G., Kim, S., Ree, J.-H., Nielsen, S.B., Billi, A., Spiess, R., 2013. Coseismic recrystallization during shallow earthquake slip. Geology 41, 63–66. https://doi.org/10.1130/G33588.1.

Smith, S.A.F., Nielsen, S., Di Toro, G., 2015. Strain localization and the onset of dynamic weakening in calcite fault gouge. Earth and Planetary Science Letters 413, 25–36. https://doi.org/10.1016/j.epsl.2014.12.043.

Smith, S.A.F., Griffiths, J.R., Fondriest, M., Di Toro, G., 2017. “Coseismic Foliations” in Gouge and Cataclasite: Experimental Observations and Consequences for Interpreting the Fault Rock Record. In: Thomas, M.Y., Mitchell, T.M., Bhat, H.S. (Eds.), Fault Zone Dynamic Processes: Evolution of Fault Properties During Seismic Rupture. Geophysical Monograph, 81–102.

Tesei, T., Collettini, C., Barchi, M.R., Carpenter, B.M., Di Stefano, G., 2014. Heterogeneous strength and fault zone complexity of carbonate-bearing thrusts with possible implications for seismicity. Earth and Planetary Science Letters 408, 307–318. https://doi.org/10.1016/j.epsl.2014.10.021.

Tesei, T., Carpenter, B.M., Giorgetti, C., Scuderi, M.M., Sagy, A., Scarlato, P., Collettini, C., 2017. Friction and scale-dependent deformation processes of large experimental carbonate faults. Journal of Structural Geology 100, 12–23. https://doi.org/10.1016/j.jsg.2017.05.008.

Trouw, R. A., Passchier, C. W., Wiersma, D. J., 2009. Atlas of Mylonites-and related microstructures. Springer Science & Business Media.

Ungár, T., 2004. Microstructural parameters from X-ray diffraction peak broadening. Scripta Materialia 51, 777–781. https://doi.org/10.1016/j.scriptamat.2004.05.007.

Verberne, B.A., Spiers, C.J., Niemeijer, A.R., de Bresser, J.H.P., de Winter, D.A.M., Plümper, O., 2014. Frictional properties and microstructure of calcite-rock fault gouges sheared at sub-seismic velocites. Pure and Applied Geophysics 31, 1–45. https://doi.org/10.1007/s00024-013-0760-0.

Verberne, B.A., Chen, J., Niemeijer, A.R., De Bresser, J.H.P., Pennock, G.M., Drury, M.R., Spiers, C.J., 2017. Microscale cavitation as a mechanism for nucleating earthquakes at the base of the seismogenic zone. Nature Communications 8. https://doi.org/10.1038/s41467-017-01843-3.

Viola, G., Mancktelow, N.S., Miller, J.A., 2006. Cyclic frictional-viscous slip oscillations along the base of an advancing nappe complex: Insights into brittle-ductile nappe emplacement mechanisms from the Naukluft Nappe Complex, central Namibia. Tectonics 25, 1–20. https://doi.org/10.1029/2005TC001939.

Violay, M.E.S., Nielsen, S.B., Gibert, B., Spagnuolo, E., Cavallo, A., Azais, P., Vinciguerra, S.C., Di Toro, G., 2014. Effect of water on the frictional behavior of cohesive rocks during earthquakes. Geology 42, 27–30. https://doi.org/10.1130/G34916.1.

Wallis, D., Phillips, R.J., Lloyd, G.E., 2013. Fault weakening across the frictional-viscous transition zone, Karakoram Fault Zone, NW Himalaya. Tectonics 32, 1227–1246. https://doi.org/10.1002/tect.20076.

Weeks, J.D., Tullis, T.E., 1985. Frictional sliding of dolomite: A variation in constitutive behavior. Journal of Geophysical Research 90, 7821-7826. https://doi.org/10.1029/JB090iB09p07821.

Williams, J.C., 1976. The segregation of particulate materials. A review. Powder Technology 15, 245-251. https://doi.org/10.1016/0032-5910(76)80053-8.

	Experiment	Experimental conditions	Target slip rate ms^{-1}	Displacement m	Normal stress MPa	Mixture batch
Single slide						
	s1210	Room humidity	0.00003	0.4	17.5	CDM1
	s1322	Room humidity	0.00003	0.1	17.5	CDM2
	s1211	Room humidity	0.0001	0.4	17.5	CDM1
	s1212	Room humidity	0.001	0.4	17.5	CDM1
	s1323	Room humidity	0.001	0.1	17.5	CDM2
	s1217	Room humidity	0.01	0.4	17.5	CDM1
	s1218	Room humidity	0.1	0.4	17.5	CDM1
	s1221	Room humidity	1	0.4	17.5	CDM1
	s1327	Water dampened	0.00003	0.05	17.5	CDM2
	s1329	Water dampened	0.00003	0.1	17.5	CDM2
	s1328	Water dampened	0.00003	0.2	17.5	CDM2
	s1214	Water dampened	0.00003	0.4	17.5	CDM1
	s1330	Water dampened	0.00003	0.4	17.5	CDM2
	s1215	Water dampened	0.0001	0.4	17.5	CDM1
	s1213	Water dampened	0.001	0.4	17.5	CDM1
	s1219	Water dampened	0.01	0.4	17.5	CDM1
	s1220	Water dampened	0.1	0.4	17.5	CDM1
	s1222	Water dampened	1	0.4	17.5	CDM1
Static load						
	sld	Room humidity			17.5	CDM1
	slw	Water dampened			17.5	CDM2

Table 1. Experiments reported in this study.

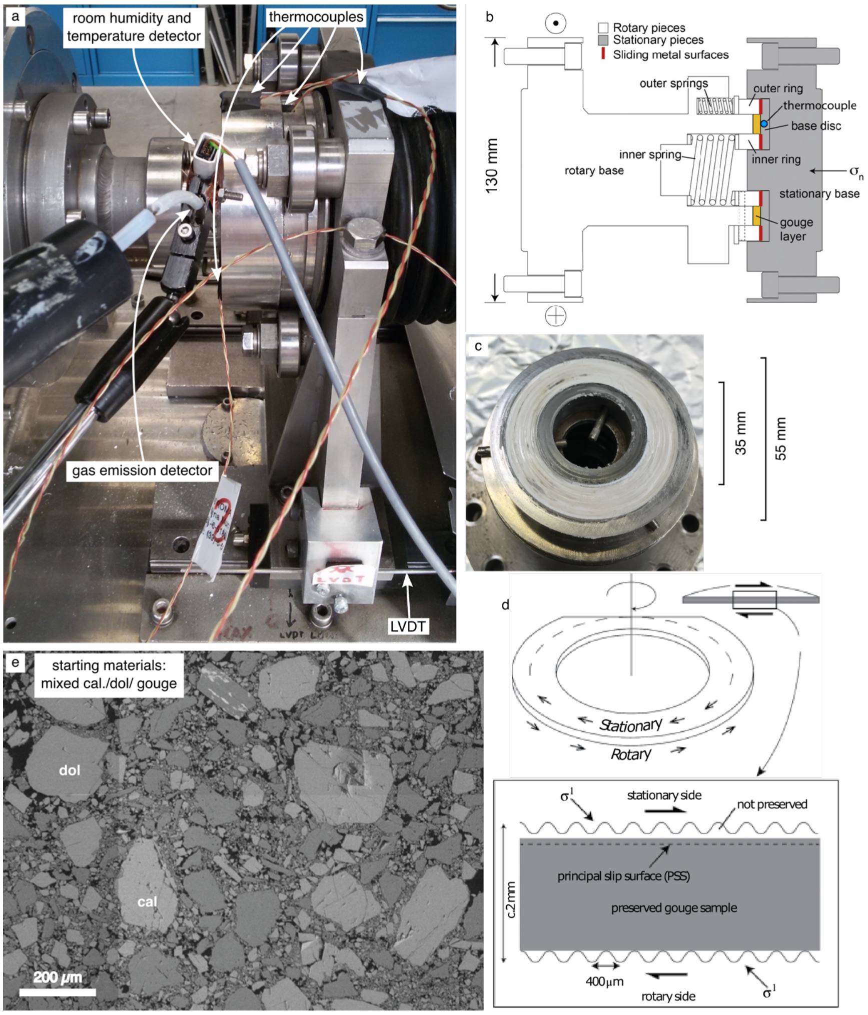

Figure 1. Rotary-shear experimental setup. a) Detectors in the sample chamber. Gas emission, humidity, and temperature detectors were placed at < 1 cm from the sample holder. Four thermocouples were placed on the stationary side at increasing distances from the gouge layer. Note: the position of the thermocouple nearest to the gouge layer is not visible here and is illustrated in b). b) Diagram of the gouge holder with the location of the thermocouple nearest to the gouge layer (modified after Smith et al., 2015). c) Sample appearance post deformation with mirror-like slip surface formed in an experiment performed at V = 0.1 ms^{-1}. d) Diagram showing the location of the recovered and analysed gouge layer after the experiment (after Smith et al., 2017). e) SEM backscattered electron (SEM-BSE) image of the starting material after applying 17.5 MPa for 300 s.

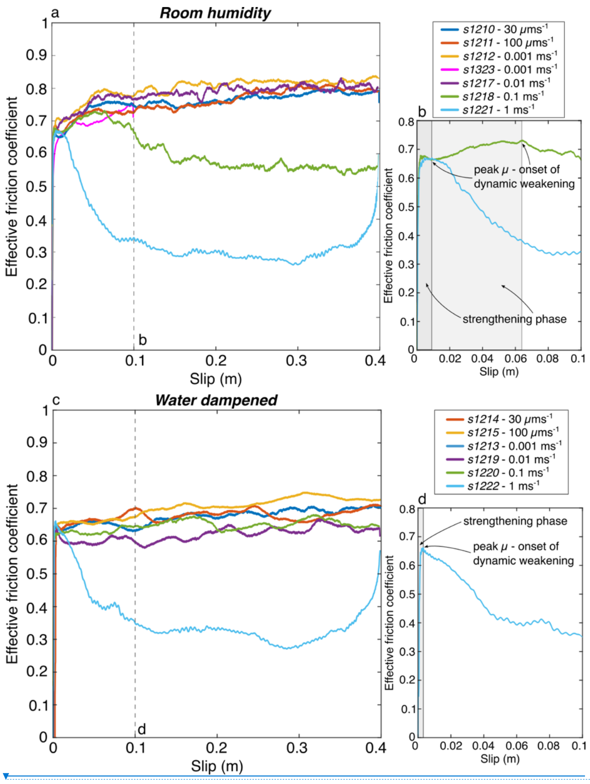

Figure 2. Effective friction coefficient in mixed calcite-dolomite gouges. a) and c) Effective friction coefficient versus slip under room-humidity and water-dampened conditions. c) and d) Detail of effective friction coefficient versus slip in the first 0.1 m of slip in experiments where slip-weakening was observed.

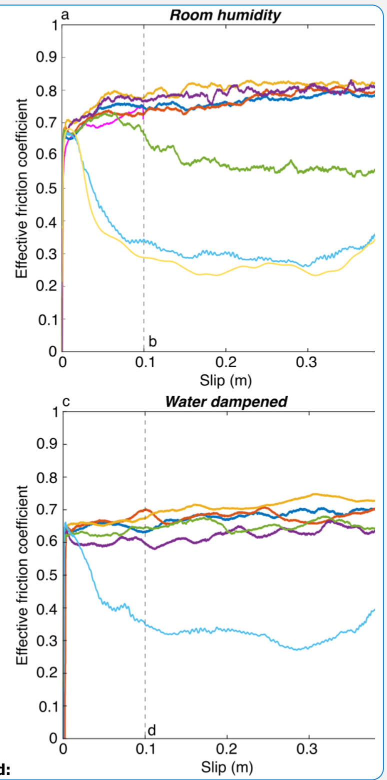

Deleted:

Deleted:

Deleted:

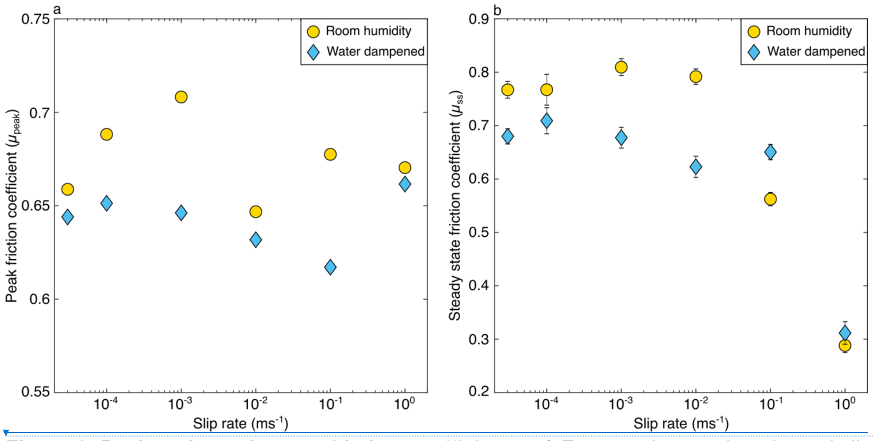

Figure 3. Peak and steady state friction coefficients. a) For experiments that showed slip strengthening, the peak friction coefficient was calculated just before the onset of strengthening behaviour in the first 0.1 m of slip. For experiments showing dynamic weakening, the peak friction immediately precedes the friction drop (see Fig. 2b and 2d). b) Steady state friction coefficient was calculated at displacements between 0.15 m and 0.35 m.

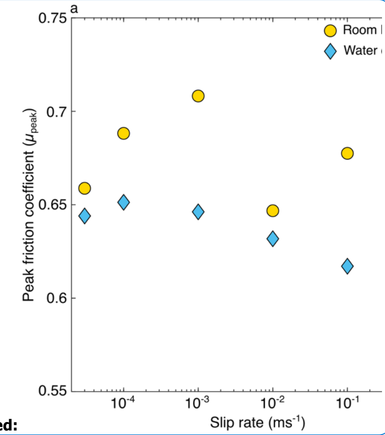

Deleted:

Deleted: coefficient

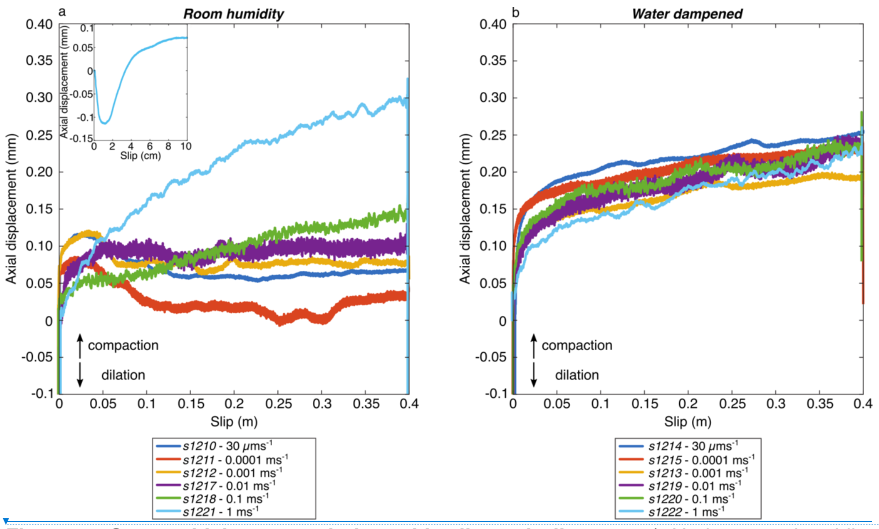

Figure 4. Gouge thickness evolution with slip and slip rate. a) Under room-humidity conditions and for slip rates of V ≤ 0.01 ms^{-1}, an initial compaction phase was followed by dilation (lasting 0.1-0.15 m) and then constant thickness. At higher slip rates (V ≥ 0.1 ms^{-1}), after a short initial dilatancy phase, the gouge compacted constantly throughout the whole experiment, with compaction rate increasing with slip rate. b) Under water-dampened conditions, the gouge compacted at a similar rate at all investigated slip rates.

Deleted:

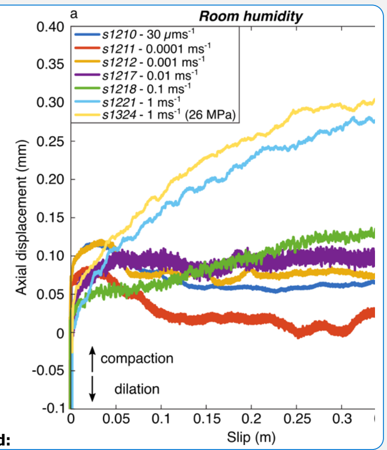

Deleted:

Deleted: phase

Deleted: was followed by a period of no compaction or dilation was observed. Instead, at

Deleted:

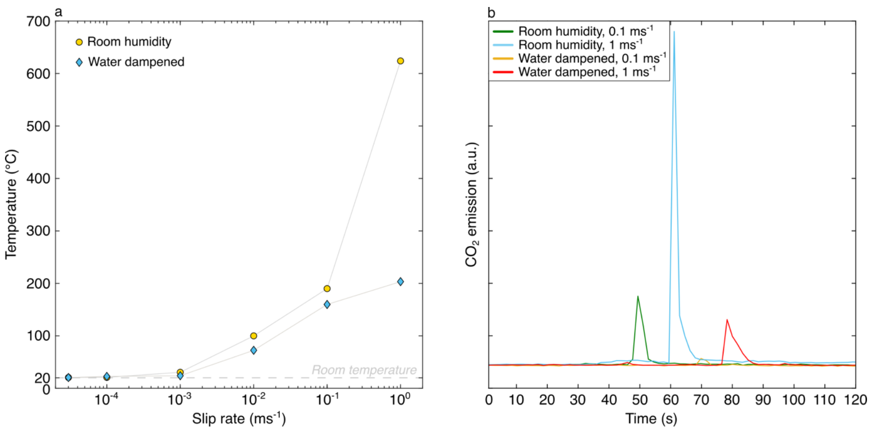

Figure 5. Peak temperatures and CO_2 emissions. a) Maximum temperature measured by the thermocouple located closest to the gouge layer (see Fig. 1b for location). b) CO_2 emissions for experiments at $V \geq 0.1$ ms^{-1} in both room-humidity and water-dampened conditions. Greater emissions occur at room-humidity conditions, but smaller and distinct peaks are also observed in the presence of water.

Deleted:

Deleted:

Deleted:

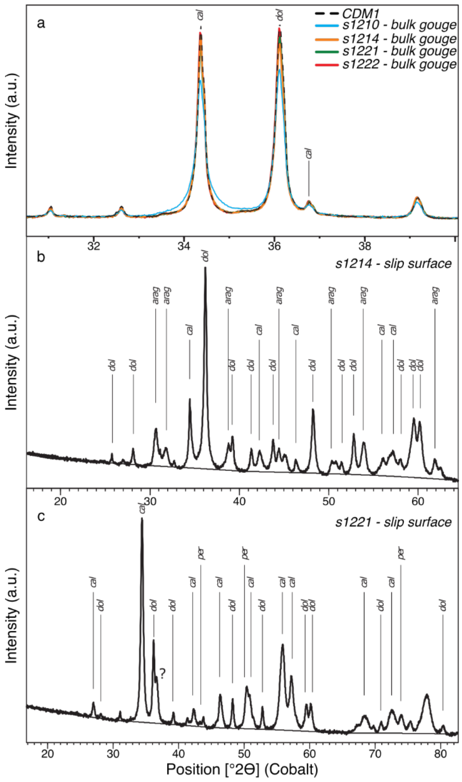

Figure 6. XRPD analysis of bulk gouge and slip surfaces. a) Bulk gouge shows a Lorentzian profile for the main calcite peak in experiment *s1210*, suggesting either a large crystallite size distribution or microstrain as a result of intense comminution involving a large fraction of the gouge. b) At 30 μms^{-1} in water-dampened conditions, traces of aragonite are found on the slip surface as a result of calcite polymorphic transformation during prolonged mechanical grinding. c) For *s1221* (1 ms^{-1} in room-humidity conditions), presence of Mg-calcite and periclase (MgO) on the mirror-like slip surface is observed due to decarbonation of dolomite.

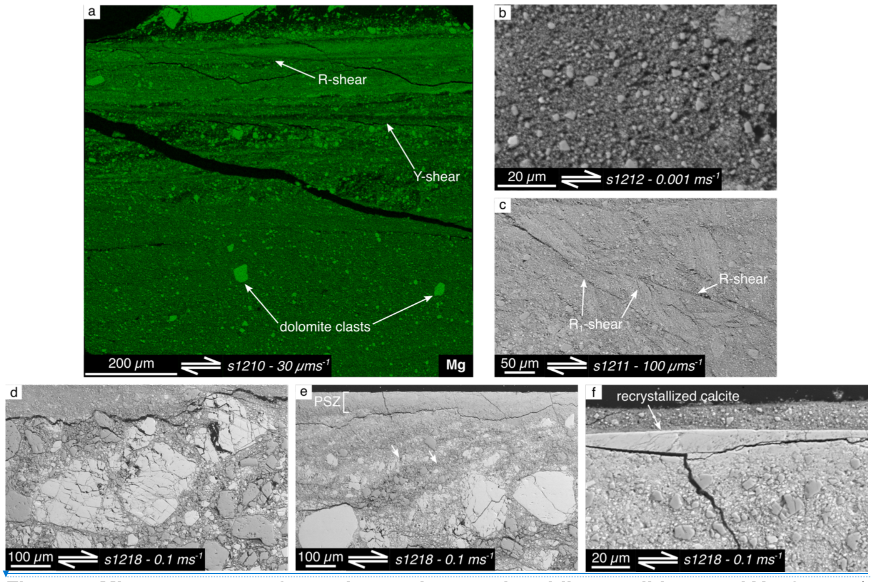

Figure 7. Microstructures of experiments in room-humidity conditions and V ≤ 0.1 ms^{-1}. a) Mg element map of the thick slip zone highlighting the location of remnant dolomite clasts. b) Detail of the fine-grained matrix in the slip zone made of a calcite-dolomite mixture with surviving sub-rounded dolomite clasts up to few tens of micrometres in size. c) The fine-grained slip zone is commonly cut by Y-, R- and R$_1$-shear bands crosscutting each other. d) Enhanced grain size reduction in calcite grains due to fracturing along cleavage planes. e) Development of a weak foliation adjacent to the principal slip zone at V = 0.1 ms^{-1}. f) Patches of dynamically recrystallized calcite along the principal slip zone at V = 0.1 ms^{-1}.

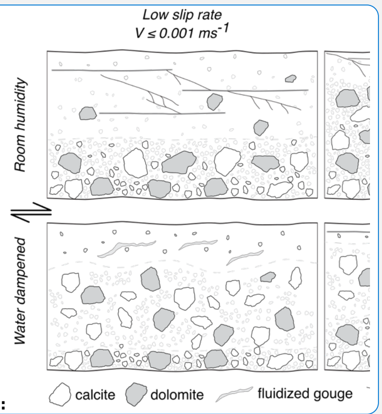

Deleted:

Moved down [9]: Summary of microstructural evolution at different slip rates and deformation conditions.

Moved down [10]: ....Page Break..........

¶

Moved down [11]: humidity conditions, partial sample loss after the experiment means slip zone thickness values are a minimum estimate.¶

..........Page Break..........

¶

Deleted: ¶

Deleted: Figure 8. Slip zone thickness evolution with slip rate and ambient conditions. The thickness of the localized slip zone decreases almost linearly with log(V) in water dampened experiments. For room

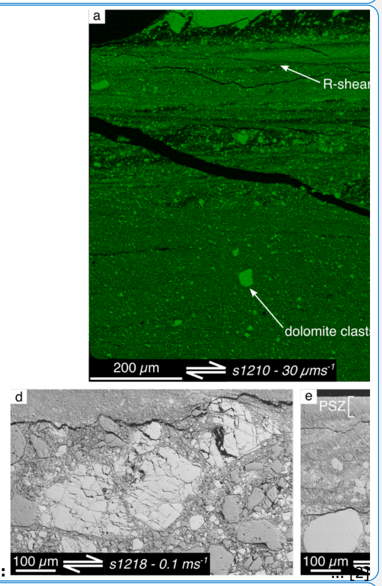

Deleted: ... [2]

Deleted:

Moved (insertion) [10]

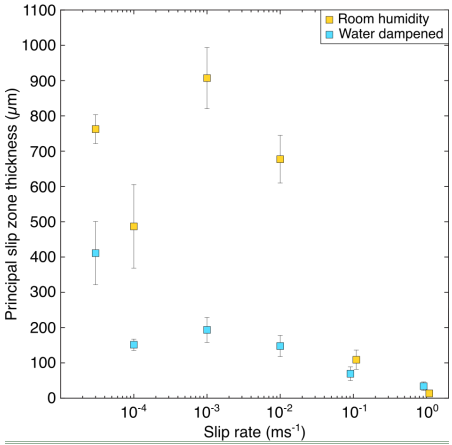

Figure 8. Slip zone thickness evolution with slip rate and presence of water. The thickness of the localized slip zone decreases almost linearly with log(V) in water-dampened experiments. For room-humidity conditions, partial sample loss after the experiment means slip zone thickness values are a minimum estimate.

Deleted: ¶

Page Break

¶

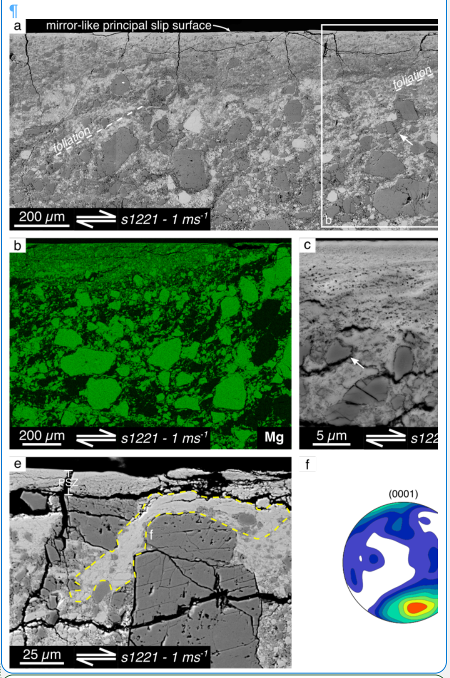

Moved (insertion) [11]

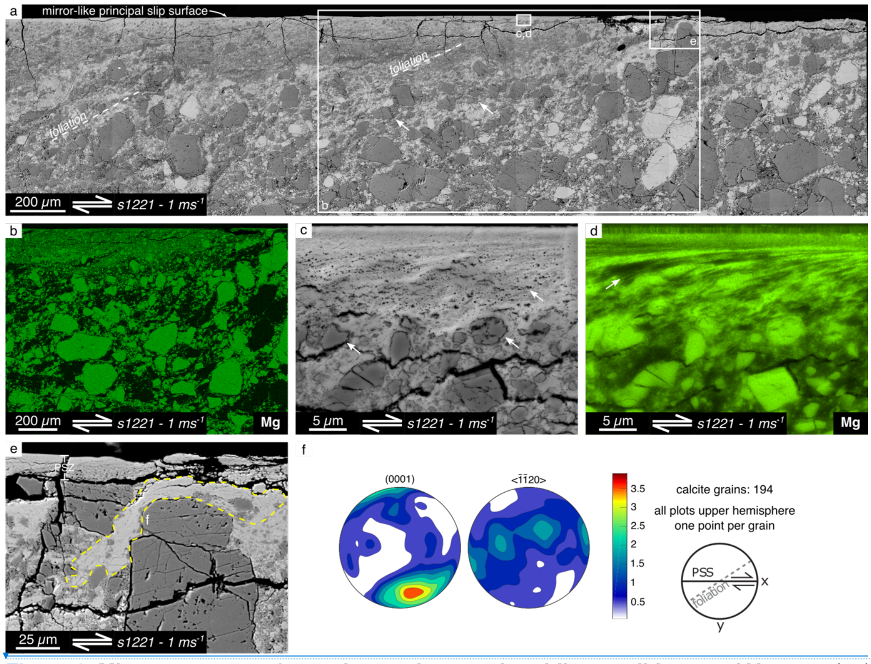

Figure 9. Microstructures of experiments in room-humidity conditions and V = 1 ms^{-1}. a) Development of a foliation consisting in alternation of calcite- and dolomite-rich domains, antithetically inclined c. 40° from the PSS and becoming subparallel to the gouge boundaries when approaching the PSS. Larger dolomite (and when present calcite) clasts have tails of fine-grained material, resembling mantled porphyroclasts. b) Mg element map highlighting foliation development in the bulk gouge. c) Dolomite clasts adjacent to the principal slip zone are characterized by internal holes and vesicular rims interpreted as due to degassing during dolomite decarbonation reaction. Banding of low and higher porosity in the principal slip zone is an indicator for dolomite content. d) Mg element map of c) showing dolomite and calcite banding in the principal slip zone. e) Transition from the principal slip zone to the underlying fractured and foliated gouge with calcite showing evidence of dynamic recrystallization. f) Orientation data for calcite in area highlighted in e). showing the development of a clear CPO along the c-axes.

Deleted: 10

Deleted:

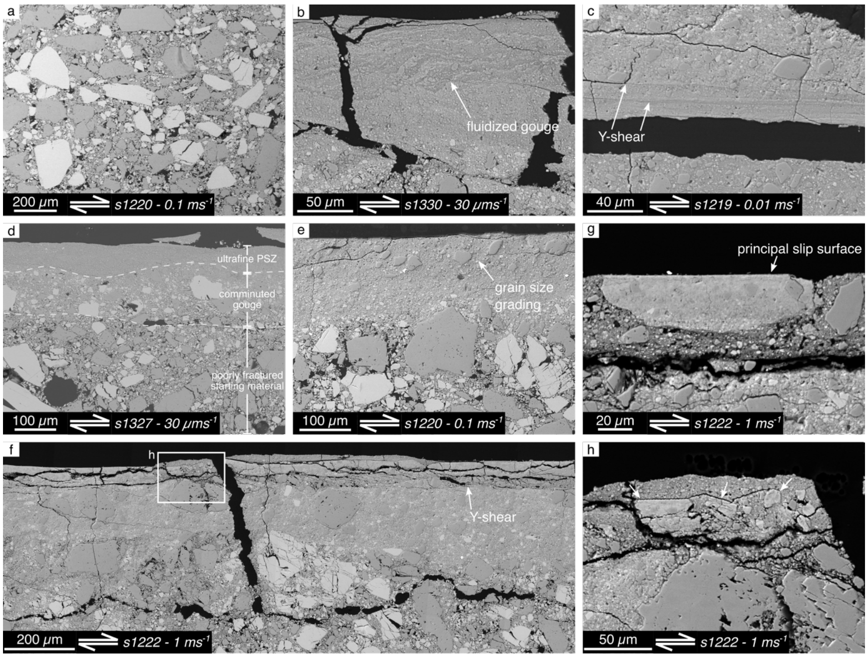

Figure 10. Microstructures of experiments in water-dampened conditions. a) The bulk gouge is made of poorly fractured calcite and dolomite mixture highly resembling the starting material. b) Occurrence of fluidized structures in the principal slip zone of experiments performed at 30 μms^{-1}. c) At 0.0001 $ms^{-1} \leq V < 0.1$ ms^{-1}, the principal slip zone is cut by multiple Y-shears. d) In the presence of fluid water, an ultrafine principal slip surface develops, overlying a highly comminuted gouge which then transitions to a poorly fractured starting material. e) At V = 0.1 ms^{-1}, grain size grading is observed in the principal slip zone, with larger clasts occurring near the principal slip surface. f) At V = 1 ms^{-1}, strain localizes on a compacted, low porosity, recrystallized slip zone, which g) is not continuous and h) often found broken and reworked.

Deleted: 11

Deleted:

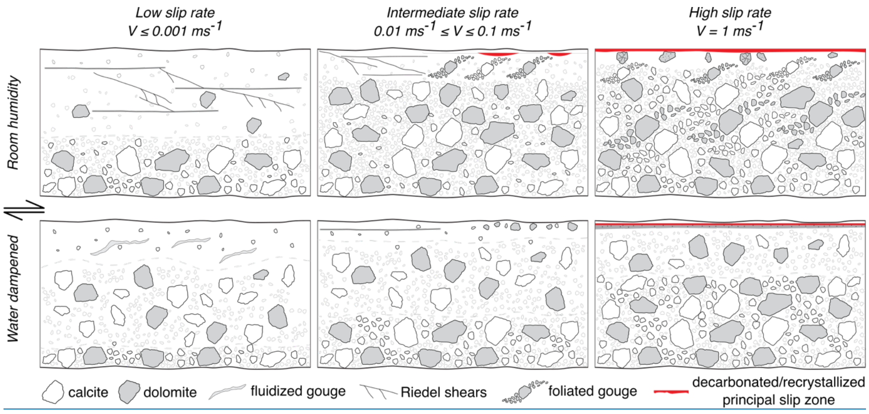

Figure 11. Summary of microstructural evolution at different slip rates and deformation conditions.

Formatted: Justified

Moved (insertion) [9]

Page 26: [1] Deleted **Author**

Page 33: [2] Deleted **Author**